ADVANCED MATERIALS
www.advmat.de

A Noninvasive and Highly Effective Inhaled Nanovaccine Based on Natural Polysaccharide for Lung Cancer Treatment

Qiang Zhang, Yu Miao, Zhike Chen, Yi Liu, Linfu Chen, Zhisheng Xiao, Hui Shen, Jingjing Shen, Feng Pan, Nanhui Liu, Xinying Lv, Haibin Zhao, Qifan Yu, Zixuan Zheng, Qian Chen, and Yang Yang**

Lung cancer is the most widespread malignancy globally and the leading cause of cancer-related deaths, highlighting the need for innovative treatments. Herein, a novel inhaled vaccine carrier is presented by modifying dextran (Dex) with *N*,*N*-dimethylethylenediamine (DMEN) and 4-(bromomethyl)phenylboronic acid (PBA) (Dex–DMEN–PBA, DDP). The optimized DDP demonstrates a potent adjuvant effect in promoting dendritic cell (DC) maturation by multiple signaling pathways. Moreover, the nanovaccine (DDP/Lewis lung carcinoma (LLC)) forms through electrostatic interactions between DDP and protein antigens derived from LLC cells. Upon inhalation, it induces DC maturation, T cell activation, and germinal center B cell activation in the thoracic lymph node. In the mouse model, the inhaled DDP/LLC nanovaccine displays impressive prophylactic effects against lung cancer, with 50% of mice alive after six months and 33% surviving a subsequent challenge, indicating strong long-term immune memory. Remarkably, it surpasses subcutaneous vaccination, particularly in activating germinal center B cells and follicular helper T (Tfh) cells, and upregulating tissue-resident memory T (T_{RM}) cells in the lung. This self-adjuvant nanovaccine effectively prevents tumor growth and induces robust immune memory, offering valuable insight for treating lung cancer and related diseases.

1. Introduction

Lung cancer ranks among the most common malignancies and continues to be the primary cause of cancer-related fatalities globally.[1,2] The latest GLOBOCAN 2022 reveals that an estimated 2.2 million new instances of lung cancer were reported (making up 12.4% of the total cancer cases), and it carries the highest cancer mortality rate (18.7%).[3] Surgical resection, often regarded as the most direct approach, is generally effective in early stage lung cancer.[4] However, its limited precision increases the risk of tumor recurrence and metastasis. Chemotherapy and radiotherapy, although widely used, lack specificity and are associated with severe side effects, resulting in poor quality of life for patients.[5] Targeted drug therapy, a promising strategy unlocked by the introduction of nanotechnology, has benefits for a small number of patients and faces the risk of being off-target.[6,7] Moreover, the heterogeneous

Q. Zhang, Y. Liu, F. Pan, Q. Yu, Z. Zheng, Y. Yang
Department of Thoracic Surgery
Shanghai Pulmonary Hospital
School of Medicine
Tongji University
Shanghai 200433, China
E-mail: timyangsh@tongji.edu.cn

Q. Zhang, Y. Yang
School of Materials Science and Engineering
Tongji University
Shanghai 201804, China

Q. Zhang, Y. Miao, Z. Chen, L. Chen, Z. Xiao, H. Shen, J. Shen, N. Liu, X. Lv, H. Zhao, Q. Chen
Institute of Functional Nano & Soft Materials (FUNSOM)
Jiangsu Key Laboratory for Carbon-Based Functional Materials & Devices
Soochow University
Suzhou 215123, China
E-mail: chenqian@suda.edu.cn

Z. Chen
Department of Thoracic Surgery
The First Affiliated Hospital of Soochow University
Suzhou 215006, China

H. Shen
Department of Thoracic Surgery
Shanghai General Hospital
Shanghai Jiao Tong University School of Medicine
Shanghai 200086, China

Y. Yang
Innovation and Incubation Center
Shanghai Pulmonary Hospital
School of Medicine
Tongji University
Shanghai 200433, China

The ORCID identification number(s) for the author(s) of this article can be found under https://doi.org/10.1002/adma.202504987

DOI: 10.1002/adma.202504987

tumor microenvironment supports tumor progression and impedes immunotherapeutic action.[8] Despite advances in these medical treatments, controlling the progression of lung cancer and reducing mortality continues to be a major challenge.[9,10]

Cancer vaccines, an innovative approach to tumor treatment, are designed by introducing tumor-specific antigens (TSAs) or tumor-associated antigens (TAAs) to trigger tumor-specific immune responses that can effectively identify and eliminate cancer cells.[11,12] Among them, mucosal vaccines have garnered a significant increase due to their ability to mimic natural infection routes.[13,14] They directly stimulate the abundant lymphatic tissue underlying mucosal surfaces, resulting in the generation of a substantial number of immunologically active cells and antibodies, which effectively thwart the invasion of pathogenic microorganisms into the body. Mucosal immunity also exhibits a "homing" phenomenon, where mature immune cells, including T and B cells, are guided by specific homing receptors to migrate not only to the sensitized site but also to other mucosal locations.[15] This process forms an extensive mucosal immune network that contributes to the development of systemic immunity throughout the body. Therefore, mucosal vaccination represents a highly efficient strategy for inducing both systemic immune protection and pathogen-specific mucosal immunity.

The lungs, with their highly developed mucosal system, are particularly well-suited for mucosal vaccination.[16–18] They are directly connected to the external environment and are populated by numerous antigen-presenting cells (APCs) in the airways, such as alveolar macrophage and dendritic cell (DC). These APCs act as vigilant sentinels, continuously surveying the environment and rapidly activating the mucosal immune response upon detecting foreign substances or antigens.[19,20] By leveraging the direct accessibility of the lung's mucosal surface and the efficiency of APCs in initiating immune responses, inhaled-based vaccination strategies stand a high probability of significantly elevating the effectiveness of vaccines, especially for lung-related diseases including lung cancer.[21,22] However, while mucosal immunity presents unique advantages, the successful development of inhaled vaccines relies on the precise and sufficient delivery of antigens to the lungs.[23] Ensuring robust activation of mucosal immune cells requires a safe and efficient delivery system capable of controlling the timing and location of tumor antigens and adjuvants.[24,25] Consequently, the development of such systems is critical for advancing inhalable mucosal vaccines for lung cancer prevention.

Dextran (Dex), a natural polysaccharide composed of glucose units, is widely used because of its biocompatible, biodegradable, easy modification, and potential immunomodulatory properties, such as enhancing surface maturation markers and increasing the production of proinflammatory cytokines.[26–28] However, its inherent hydrophilic nature leads to rapid elimination from the body, resulting in low and unstable antigen loading efficiency, as well as challenges related to endocytosis and antigen presentation capabilities. Although extensive research has been conducted on chemically modified dextran-based antigen delivery systems, such as acid-sensitive acetylated dextran, reactive-oxygen-species-responsive boronate dextran, these primarily focus on enhancing antigen presentation efficiency via microenvironment-responsive architectures.[29–31] Nevertheless, challenges such as limited antigen loading capacity and suboptimal immune activation efficiency persist. In this study, we developed a novel cationic dextran with excellent self-adjuvant peculiarity, serving as a potent inhaled nanovaccine to elicit strong and comprehensive immune responses for preventing lung cancer invasion (**Scheme 1**). The natural polysaccharide dextran was modified with *N*,*N*-dimethylethylenediamine (DMEN) and 4-(bromomethyl)phenylboronic acid (PBA) to create a potential cationic carrier (Dex–DMEN–PBA, DDP). The functional performance of DDP was optimized by fine-tuning the feed ratio of DMEN and PBA. Remarkably, DDP with 50% PBA substitution exhibited the most potent effect in stimulating the maturation of mouse bone marrow-derived dendritic cells (BMDC). RNA transcriptomic sequencing analysis (RNA-seq) revealed that DDP drives DC maturation through multiple signaling pathways among which cytokine–cytokine receptor interactions, chemokine signaling pathways, Toll-like receptor (TLR) signaling pathway, tumor necrosis factor (TNF) signaling pathways, the nuclear factor kappa B (NF-κB) signaling, and other related inflammatory pathways, thereby triggering robust immune responses. Moreover, the assembled nanovaccine was formed through electrostatic interactions between DDP and antigens including model antigen OVA or antigens derived from the Lewis lung carcinoma (LLC) cells. This nanovaccine exhibited excellent performance in promoting antigen cross-presentation, mediated by multiple pathway-driven endocytosis mechanisms, including clathrin-mediated endocytosis, cholesterol-dependent endocytosis, and energy-dependent mechanisms. Furthermore, mice immunized with the DDP/LLC nanovaccine displayed outstanding prophylactic effects following exposure to LLC tumor cells. Compared to other groups, the DDP/LLC group significantly extended the lifespan, with even 50% of LLC-bearing mice still alive half a year later. Furthermore, 33% of these survivors still exhibited strong long-term immune memory effects against rechallenged LLC cells. More interestingly, compared to classical subcutaneous vaccination route, the inhaled immunization strategy demonstrated superior advantages in promoting germinal center B cell maturation and follicular helper T (Tfh) cell activation in the thoracic lymph node. Additionally, it upregulated the number of tissue-resident memory T cells (T_{RM}) in the lungs, further enhancing immune responses. Therefore, our work presents a novel and simple strategy based on a self-adjuvant carrier for spatial and temporal delivery of antigens via inhalation, providing valuable insight into the development of vaccines against lung-related diseases in the clinic.

2. Results and Discussion

2.1. Synthesis and Characterization of DDP

The synthesis of DDP is illustrated in **Figure 1a** and involves a three-step process. First, the intermediate product Dex–DMEN (DD) was synthesized by activating the hydroxyl groups of dextran using 1,1′-carbonyldiimidazole (CDI), followed by a reaction with DMEN. In the subsequent step, a grafting reaction between Dex–DMEN and PBA occurred, resulting in the formation of the final product, DDP. DDP with different modification ratios could be synthesized by adjusting the feed ratios of DMEN and PBA. The efficiency of DDP modification was evaluated by ^{1}H nuclear magnetic resonance (NMR) (Figure 1b and Table S1

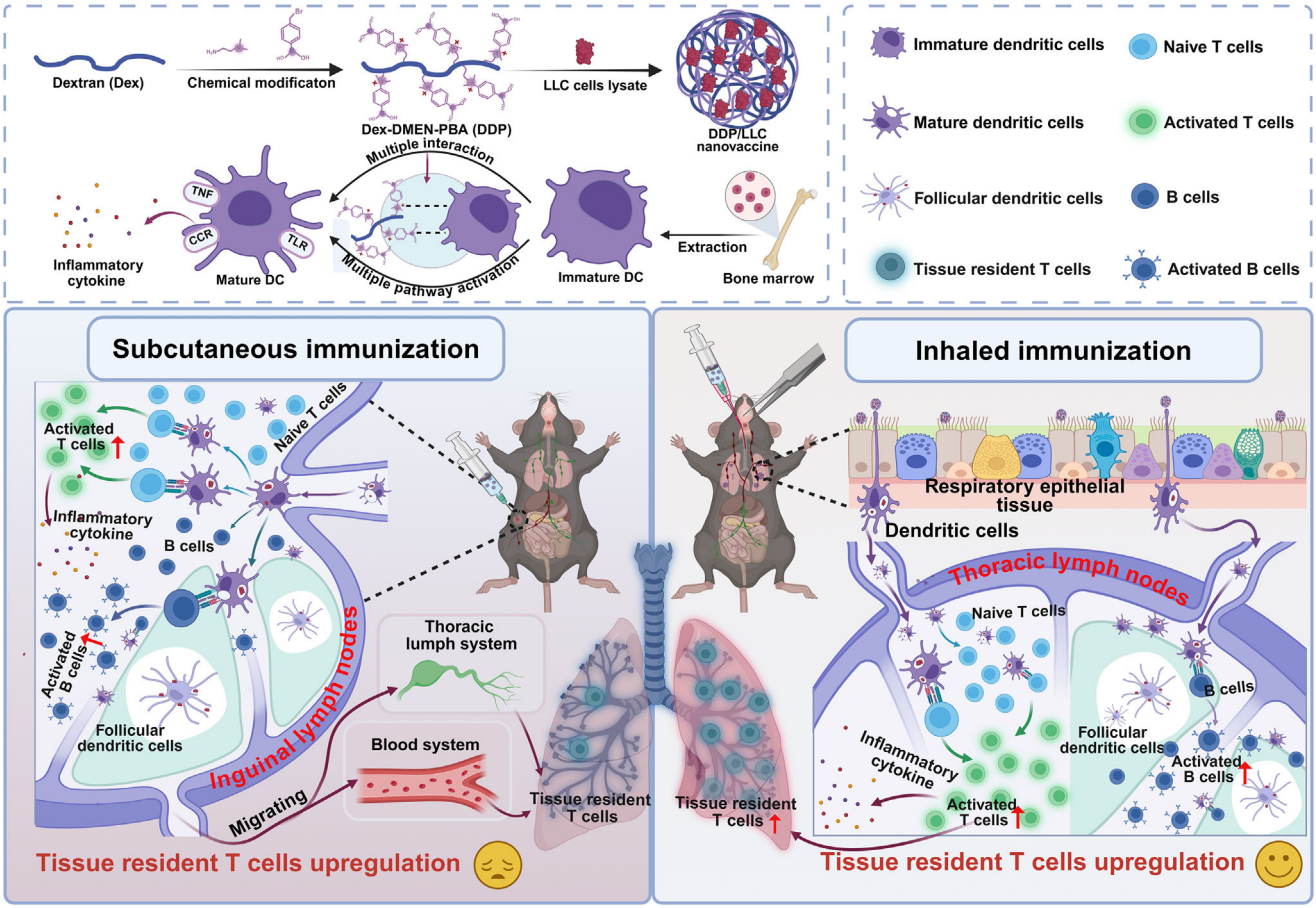

Scheme 1. Schematic illustration of DDP/LLC nanovaccine designed to prevent the progression of lung cancer. a) Natural dextran was modified into a novel vaccine vector (DDP) for delivering the LLC lysate antigen, the optimal DDP demonstrated the ability to stimulate BMDC maturation by multiple signaling pathways activation. b) The resulting DDP/LLC nanovaccine exhibits remarkable potential to activate immune response, thereby preventing lung cancer progression by inhaled immunization. Compared to traditional subcutaneous immunization, this inhaled immunization strategy demonstrated significant advantages in promoting the maturation and activation of germinal center B cells and Tfh cells in the thoracic lymph node, as well as the upregulation of T_{RM} cells in the lung. Illustration created in BioRender.

(Supporting Information)). As is clearly illustrated in Figure 1b, the ^{1}H NMR spectrum of DDP displays characteristic proton signal peaks for DMEN at δ 1.92 and for PBA at δ 7.56 and 7.85. The degree of grafting for BPA was calculated by analyzing the integral intensities of the characteristic signal peaks of dextran (δ 5.12) and BPA (δ 7.56, 7.85). In addition, Fourier transform infrared (FT-IR) spectroscopy revealed a prominent peak at 1693 cm^{-1} corresponding to C═O stretching vibrations and characteristic peaks between 1500 and 1600 cm^{-1} attributed to C═C skeletal vibrations, further confirming the successful modification of DDP (Figure 1c).

With the successful synthesis of DDP with different PBA substitutions (labeled DDP25, DDP50, and DDP100), we then investigate their cellular uptake efficiency. Briefly, DC 2.4 cells were incubated with DDP/bovine serum albumin (BSA)– fluorescein isothiocyanate (FITC) nanoparticles (DDP25, DDP50, and DDP100 assembled with BSA–FITC) with the same BSA concentration at 20 μg mL^{-1} for 4 h, and the cellular uptake was performed by flow cytometry. As is graphically depicted in Figure 1d, the endocytosis gradually increased with higher PBA substitution, which may be attributed to the higher zeta potential resulting from the higher degree of substitution. Next, the immunostimulatory effects of DDP25, DDP50, and DDP100 (all at 20 μg mL^{-1}) were investigated. The results revealed that the expression of critical maturation markers, CD80 and CD86, on BMDC was upregulated to varying extents after incubation with different materials. Among these, DDP50 showed the most potent stimulatory effect when compared to both DDP100 and DDP25 (Figure 1e,f). Furthermore, DDP50 exhibited lower cytotoxicity, even at higher concentrations, compared with DDP100 (Figure 1g). Therefore, DDP50 was adopted for the following experiments without additional specifications.

To further validate the rationale behind the material design, the endocytosis and immunostimulatory effects of different modifications including intermediate products (DD), phenylboronic-acid-conjugated dextran (Dex–PBA, DP) (Figure S1, Supporting Information), were compared. According to the results in Figure 1h, the Dex and DP groups showed minimal cellular uptake behavior, and the performance of DD was somewhat improved but still fell short of expectations. This could be

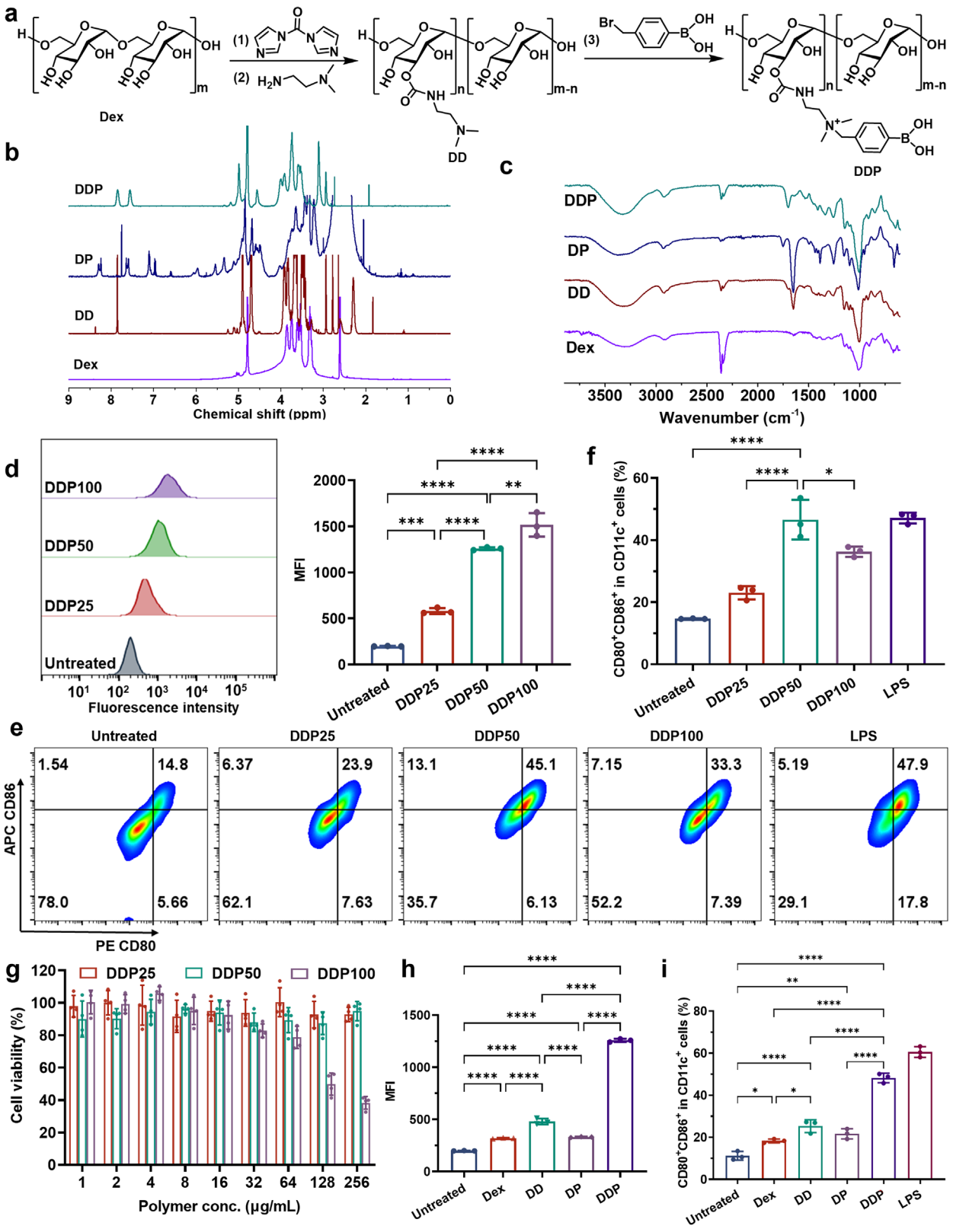

attributed to its weak protein assembly ability in these carriers. Encouragingly, the DDP group demonstrated extremely superior cellular endocytosis, far surpassing the other groups, indicating that DDP significantly enhances the intracellular delivery of the cargo, likely caused by its multiple factors of the introduced phenylboronic acid group through nitrogen–boronate complexation, cation–π interactions, and classical electrostatic interactions.[32,33] In addition, a similar result was observed in BMDC maturation experiment. Only the DDP group showed excellent BMDC maturation after incubation with BMDC for 24 h (Figure 1i), while the other groups exhibited a notable gap in stimulating BMDC maturation. The pronounced difference in this effect may be attributed to the transformation of the tertiary amine in DD into its quaternary ammonium form upon the addition of PBA. This structural modification not only enhances the charge effect but also strengthens the protein interactions mediated by PBA.[30,34,35] Together, these factors significantly amplify the functionality of DDP.

2.2. Immune Activation Mechanism of DDP

Building on the observed immunostimulatory effect of DDP, we further performed RNA transcriptomic analysis to systematically investigate the specific pathways by which DDP promotes BMDC maturation (**Figure 2a**). The principal component analysis results are shown in Figure S2 (Supporting Information). The volcano plot highlights significant changes in gene expression following DDP treatment, with 941 genes showing notable upregulation and 962 genes experiencing significant downregulation (adjusted p values < 0.01) (Figure 2b). Specifically, BMDC treated with DDP exhibited an upregulation in genes associated with BMDC maturation, including those involved in TNF signaling, interferon signaling, interleukins and receptors signaling, chemokines and receptors signaling, and TLR signaling pathways, compared to the untreated BMDC (Figure 2c). Gene Ontology (GO) and Kyoto Encyclopedia of Genes and Genomes (KEGG) enrichment analyses further underscored the differential gene expression between DDP-treated or untreated BMDC, pinpointing key pathways manifested in cytokine–cytokine receptor interactions, chemokine signaling, TLR signaling, TNF signaling, and NF-κB signaling (Figure 2d,e). Moreover, the differential genes enriched in these pathways were presented in Figure 2f. These pathways are critical in immune cell activation and inflammation, highlighting the immune-modulatory potential of DDP.

To validate the RNA-seq results, quantitative real-time polymerase chain reaction (qPCR) was implemented to determine the mRNA expression levels of key molecules in these pathways in BMDC treated with DDP. The qPCR results were consistent with the RNA-seq findings, showing a marked upregulation in the expression of interleukin 6 (IL-6), CD80, chemokine (C—C motif) ligand 12 (CCL12), and TNF receptor superfamily member 9 (TNFSF9) (Figure 2g–j), indicating that DDP induces BMDC maturation by activating multiple signaling pathways. Taken together, these results collectively support that DDP could successfully activate the immune system through the coordinated activation of a range of key immune pathways, providing a strong foundation for its selection as a candidate for subsequent experiments.

2.3. In Vitro Immunostimulatory Effects of the Assembled DDP/OVA Vaccine

Building on the robust adjuvant properties of DDP, we assessed its immunostimulatory effects on BMDC with different dosages. As illustrated in Figure S3a (Supporting Information), it is evident that 20 μg mL^{-1} of DDP is optimal for immunostimulation. At this concentration, we loaded the model antigen OVA at final concentrations of 10, 20, and 40 μg mL^{-1} to assess its effect on antigen cross-presentation. The results demonstrated that the expression of the surface marker SIINFEKL^{+} peptide on BMDC reached saturation when the OVA concentration increased to 20 μg mL^{-1} (Figure S3b, Supporting Information). Based upon result, we designed a nanovaccine, DDP/OVA, by loading the model antigen OVA onto the optimized DDP at a 1:1 weight ratio through simple physical mixing (**Figure 3a**). The loading efficiency of OVA was determined to be 97.7%, as measured using bicinchoninic acid (BCA) kit (Table S2, Supporting Information). The resulting DDP/OVA nanovaccine was characterized using dynamic light scattering as well as transmission electron microscope (TEM) (Figure 3b). The DDP/OVA nanovaccine exhibited an average size of ≈120 nm and was uniformly dispersed. Notably, compared to free DDP, DDP/OVA exhibited a notable decrease in zeta potential, likely attributed to the strong electrostatic interactions between OVA and DDP (Figure S4, Supporting Information). Despite the high positive surface charge, which initially suggested potential stability challenges, the DDP/OVA nanovaccine demonstrated excellent stability in phosphate-buffered saline (PBS) (Figure S5, Supporting Information). UV–visible absorbance spectra of free OVA, DDP, and DDP/OVA further confirmed the successful coassembly of OVA and DDP into nanoparticles. A characteristic absorbance peak at 280 nm, corresponding to both DDP and OVA, was significantly enhanced in the DDP/OVA spectrum, reinforcing the successful coassembly of the two components (Figure S6, Supporting Information). To investigate whether OVA maintained its structural integrity after coassembly with DDP, we measured the circular dichroism (CD) spectra of free OVA and DDP/OVA nanoparticles. As expected, the CD spectrum of DDP/OVA closely resembled that of free OVA, indicating that the electrostatic interactions

Figure 1. Synthesis and characterization and Functionality of DDP. a) Schematic representation of the synthesis route for DDP. b) ^{1}H NMR spectra of Dex, DD, Dex–PBA (DP), and DDP. c) FT-IR spectra of Dex, DD, DP, and DDP. d) Representative flow cytometry diagram and the corresponding statistical data showing the cellular uptake efficiency of DC 2.4 cells after incubation with nanoparticles with different PBA substitutions ($n = 3$). e) Representative flow cytometry diagram and f) the corresponding statistical data showing the maturation of BMDC after incubation with nanoparticles with different PBA substitutions ($n = 3$). g) Cytotoxicity of DDP with different PBA substitutions after 24 h coincubation with DC2.4 cells ($n = 4$). h) Statistical data showing the cellular uptake efficiency of DC 2.4 cells after incubation with dextran with different modifications ($n = 3$). i) Statistical data showing the maturation of BMDC after incubation with dextran with different modifications ($n = 3$). Data are presented as the mean ± standard deviation (SD) ($n = 3$). Statistical significance was calculated via one-way ANOVA (panels d, f, h and i) in GraphPad Prism. * $p < 0.05$, ** $p < 0.01$, *** $p < 0.001$, and **** $p < 0.0001$.

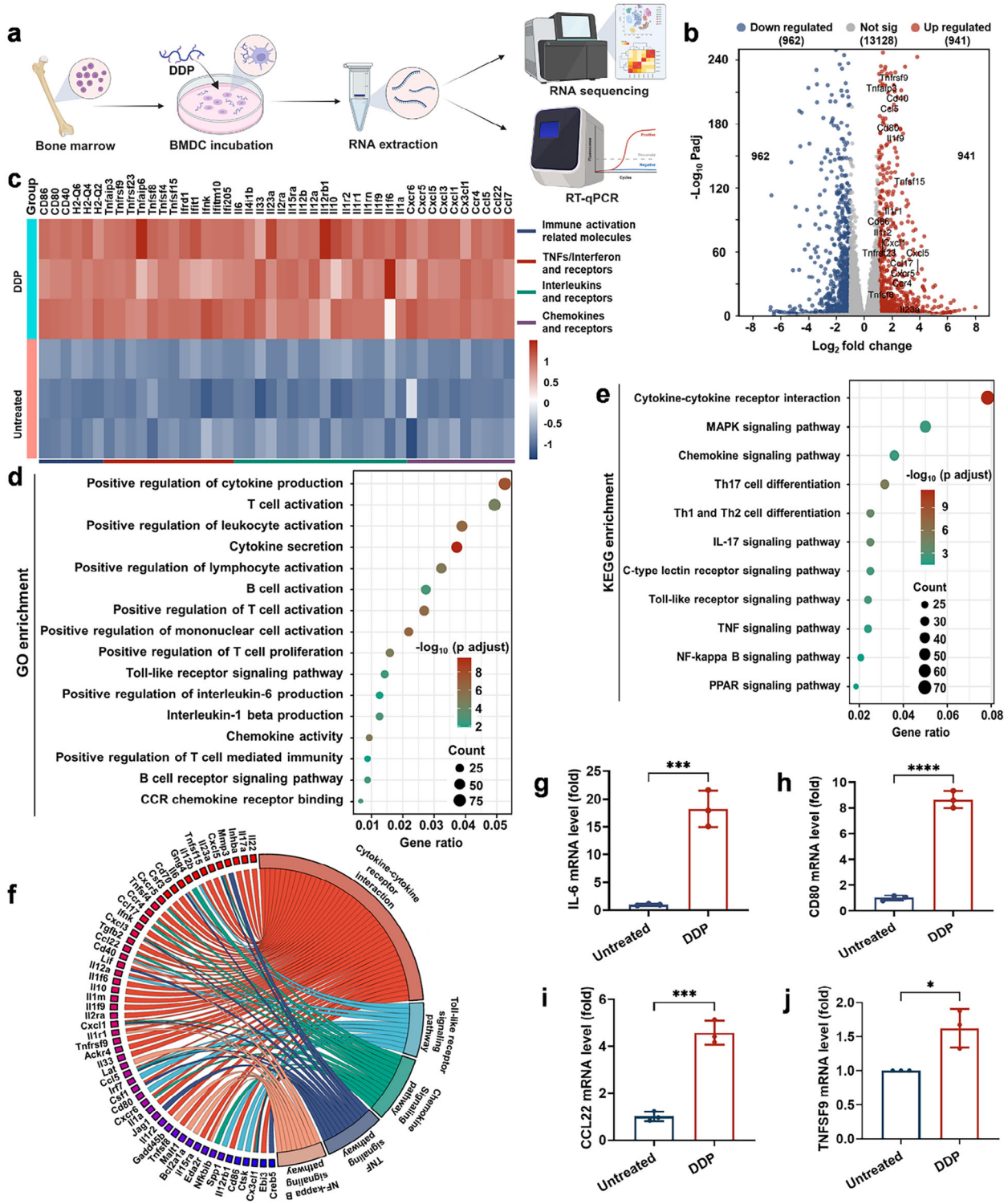

Figure 2. Mechanism of immune activation induced by DDP. a) Schematic illustration depicting the process by which DDP-treated BMDC were analyzed by RNA transcriptome sequencing and qPCR. b) Volcano plot of differentially expressed genes after DDP treatment compared to untreated controls. Genes significantly upregulated or downregulated are indicated in red and blue, respectively (false discovery rate (FDR)-adjust ed p ($p$adj) value < 0.01 and log2 (fold change) > 1). c) Cluster heatmap showing the transcript expression of related genes in DDP-treated versus untreated samples. d) GO enrichment analysis and e) KEGG pathway enrichment analysis showing differentially expressed genes after DDP treatment compared to untreated controls. f) Chord diagram representing the enriched differential genes associated with specific pathways. g–j) mRNA expression levels of key molecules, including IL-6, CD80, CCL22, and TNFSF9, were quantified by qPCR ($n = 3$). Data are presented as the mean ± SD ($n = 3$). Statistical significance was calculated via two-sided unpaired t-tests (panels g–j) in GraphPad Prism. * $p < 0.05$, ** $p < 0.01$, *** $p < 0.001$, and **** $p < 0.0001$.

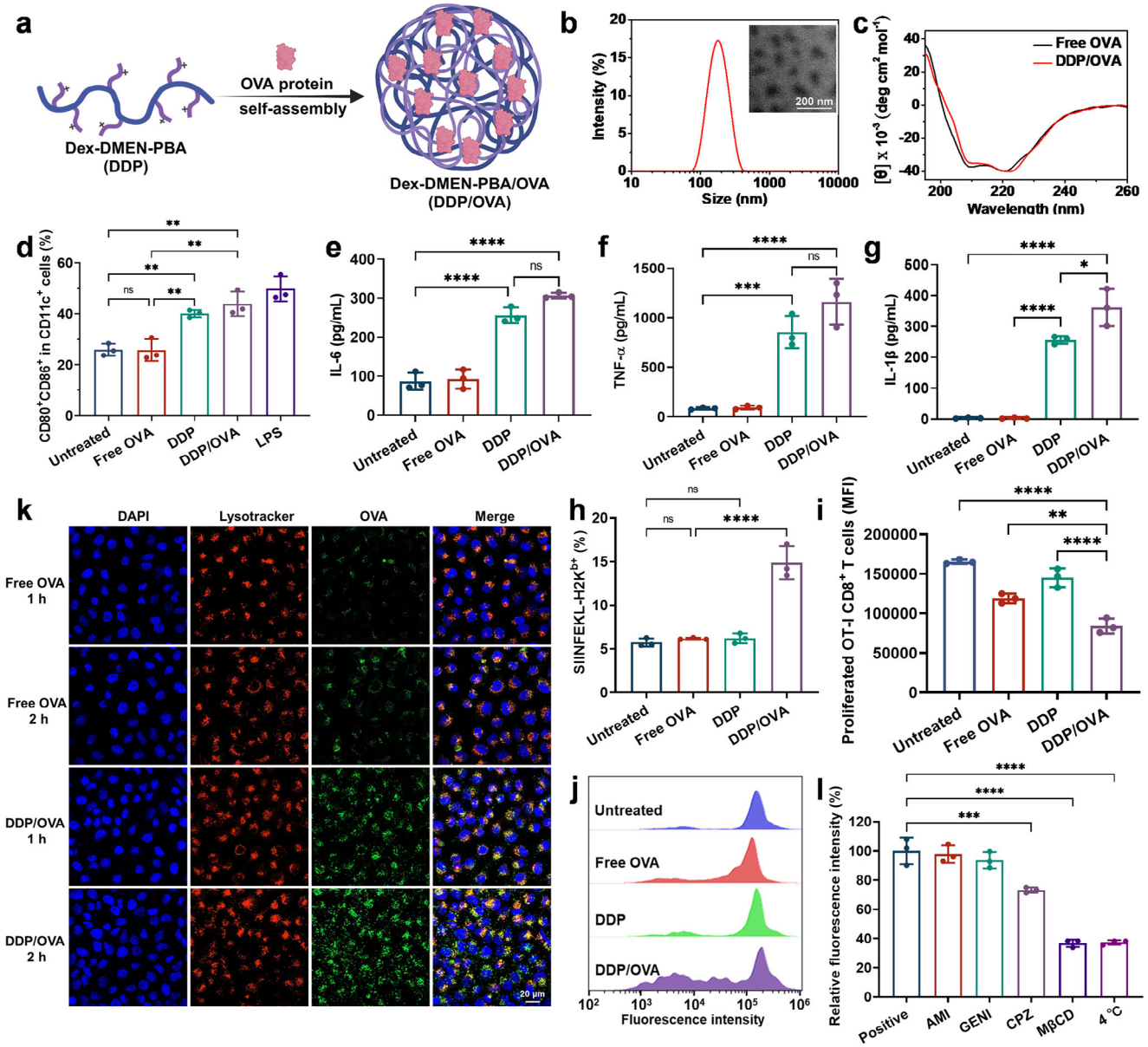

Figure 3. Preparation and characterization of the assembled DDP/OVA vaccine. a) Scheme diagram illustrating the assembly of DDP/OVA vaccine. b) Size distribution of the assembled DDP/OVA vaccine, with an inset showing a TEM image. c) CD spectra of free OVA and the assembled DDP/OVA vaccine. d) Statistical data showing the percentages of $CD86^+CD80^+$ BMDC after different treatments ($n = 3$). The concentrations of e) IL-6, f) TNF-α, and g) IL-1β in the supernatant of BMDC with different treatments ($n = 3$). h) The proportions of SIINFEKL-$H2K^{b+}$ presenting BMDC after different treatments ($n = 3$). i) Statistical data and j) representative diagram showing the proliferation of OT-I $CD8^+$ T cells after incubation with BMDC with different pretreatments ($n = 3$). k) CLSM images of DC2.4 cells treated with free FITC–OVA or the assembled DDP/FITC–OVA vaccine for 1 and 2 h. Cell nuclei and lysosomes were stained with DAPI (blue) and LysoTracker red (red), respectively. Scale bars were 20 μm. l) Relative mean fluorescence intensity of DC2.4 cells pretreated with various endocytosis inhibitors or at 4 °C, followed by incubation with the assembled DDP/OVA vaccine for 4 h ($n = 3$). Data are presented as the mean ± SD ($n = 3$). Statistical significance was calculated via one-way ANOVA (panels d–g, h, i, and l) in GraphPad Prism. * $p < 0.05$, ** $p < 0.01$, *** $p < 0.001$, and **** $p < 0.0001$.

between OVA and DDP did not affect the secondary structure of OVA (Figure 3c).

Based on the above screening and verification results, we following comprehensive comparison of the immunostimulatory effects of free OVA (20 μg mL^{-1}), DDP (20 μg mL^{-1}), and DDP/OVA (DDP: 20 μg mL^{-1}, OVA: 20 μg mL^{-1}), with lipopolysaccharides (1 μg mL^{-1}) used as the positive control. After incubating BMDC with these materials for 24 h, cell maturation was assessed by flow cytometry. The results revealed that free OVA had minimal ability to activate the expression of critical maturation markers CD80 and CD86 on BMDC, whereas DDP and DDP/OVA demonstrated strong stimulation effects, significantly upregulating the expression levels of CD80 and CD86 (Figure 3d). Moreover, the value of cytokines related to

inflammation in the supernatant of BMDC following the treatments was quantified via enzyme-linked immunosorbent assay. As exhibited in Figure 3e–g, free OVA elicited very little secretion of proinflammatory factors including TNF-α, IL-6, and interleukin-1beta (IL-1β). By contrast, DDP significantly triggered the secretion of substantial amounts of inflammatory factors, and the DDP/OVA generated even higher levels of cytokine secretion, particularly IL-1β. Given the importance of efficient antigen processing and presentation by APCs in initiating immune responses, we further investigated the expression of the surface marker SIINFEKL$^+$ peptide on BMDC after coincubation with free OVA (20 μg mL^{-1}), DDP (20 μg mL^{-1}), or DDP/OVA (DDP: 20 μg mL^{-1}, OVA: 20 μg mL^{-1}) for 24 h.[36,37] We observed that the SIINFEKL$^+$ peptide expression on BMDC was significantly enhanced in the DDP/OVA group, with levels higher than those in the free OVA group (Figure 3h). This result indicated that BMDC could effectively process and present antigens on its surface. In addition to antigen processing and presentation, the subsequent presentation of antigens to T cells and their activation is a crucial step in the vaccine process.[38] To evaluate this, free OVA (20 μg mL^{-1}), DDP (20 μg mL^{-1}), or DDP/OVA (DDP: 20 μg mL^{-1}, OVA: 20 μg mL^{-1}) was preincubated with BMDC for 24 h. Then, splenic T cells from OT-I mice (prelabeled with CFSE) were cocultured with these BMDC with pretreatment for 72 h and analyzed by flow cytometry. We found that free OVA had only a minimal effect on T cells proliferation, consistent with above results. By contrast, the DDP/OVA-treated group significantly enhanced antigen-specific T cell proliferation and differentiation, which may be attributed to more efficient antigen presentation by BMDC, thereby promoting T cell activation (Figure 3i,j). Notably, although DDP alone could stimulate BMDC maturation, the absence of antigen limited its capacity to effectively induce T cell proliferation.

Inspired by the strong immune responses induced by DDP/OVA, we further explored the endocytic pathway of the nanovaccine using FITC-labeled OVA as the model antigen. Briefly, DC 2.4 cells were incubated with either free FITC–OVA (OVA: 20 μg mL^{-1}) or DDP/FITC–OVA (FITC–OVA: 20 μg mL^{-1}, DDP: 20 μg mL^{-1}) for 1 or 2 h. After staining with 4′,6-diamidino-2′-phenylindole (DAPI) and LysoTracker Red, the cells were imaged by confocal laser scanning microscopy (CLSM). As graphically depicted in Figure 3k, the DDP/FITC–OVA-treated group showed substantial endocytosis of FITC–OVA within 1 h, with a noticeable green fluorescence signal that did not colocalize with the red fluorescence of lysosomes. By contrast, free FITC–OVA exhibited poor cellular uptake, with its green fluorescence largely overlapping with the red fluorescence of lysosomes. This phenomenon was even more pronounced after a 2 h incubation, indicating that DDP/OVA could efficiently bypass protein inactivation caused by inefficient lysosome escape, thereby improving intracellular delivery.[37] These results strongly support the superior antigen cross-presentation ability of the DDP/OVA nanovaccine.

Intrigued by the remarkable efficiency of cytosolic delivery, we further investigated the endocytic mechanism of DDP/FITC–OVA. DC 2.4 cells were pretreated with various endocytic inhibitors including micropinocytosis inhibitors (amiloride hydrochloride, AMI), clathrin-mediated endocytosis inhibitors (chlorpromazine, CPZ), tyrosine kinase inhibitors (genistein, GENI), cholesterol-dependent endocytic inhibitors (methyl-β-cyclodextrin, MβCD), or exposed to 4 °C (inhibits energy-dependent endocytosis) for 2 h, followed by the addition of DDP/FITC–OVA for 4 h. After that, flow cytometry was employed to analyze the cells. The results revealed that in the AMI- and GENI-treated groups, the fluorescence intensity remained largely unchanged compared to the positive control, indicating that the efficient endocytosis of DDP/OVA was not mediated by macropinocytosis or caveolae-dependent endocytosis (Figure 3l). However, in the CPZ-, MβCD-, and 4 °C-treated groups, the fluorescence signal was markedly reduced compared to the positive control, indicating that the cellular uptake of DDP/OVA occurs via multiple pathways, including clathrin-mediated endocytosis, cholesterol-dependent endocytosis, and energy-dependent mechanisms.

2.4. Immune Evaluation and Prophylactic Effect of Inhalable DDP/LLC Nanovaccine

The development of prophylactic cancer vaccine hinges on two key aspects: antigen selection and delivery systems. TSAs and neoantigens precisely trigger tumor-specific immunity with low tolerance risk. However, their scarcity and the challenges in identification limit their widespread application. TAAs, while facing challenges such as high immune tolerance and weaker specificity, offer broader coverage for the development of universal vaccines. Carrier-mediated codelivery of antigens and adjuvants prolongs antigen presentation, thereby enhancing sustained T/B cell activation for durable immunity. Inspired by the effective immunostimulatory effect of DDP/OVA vaccine, we explored the use of cell lysates from LLC cells—commonly used in lung cancer research—as a comprehensive antigen for developing a protective nanovaccine against lung cancer.[39,40] The preparation of DDP/LLC nanovaccine followed the same procedure as for DDP/OVA, with the only difference being the substitution of the antigen protein with LLC cell lysate (**Figure** 4a). Similar to DDP/OVA, the assembled DDP/LLC nanovaccine exhibited monodisperse nanoparticles with a particle size of ≈200 nm (Figure S7, Supporting Information). Given the unique microenvironment of the lungs, we adopted an inhalational immunization strategy to evaluate its immunological activation effects for the following in vivo experiment. Briefly, mice were vaccinated via inhalation with DDP (20 μg per mouse), LLC lysate protein (20 μg per mouse), or DDP/LLC (20 μg DDP and 20 μg LLC lysate protein per mouse) on days −35, −21, and −7. One week after the third immunization (day 0), the mice were euthanasia, and their thoracic lymph nodes, lungs, and spleens were acquired for immunological analysis by flow cytometry. The detailed immunization timeline is illustrated in Figure 4b. As expected, similar to the in vitro BMDC maturation, both DDP and DDP/LLC effectively stimulated the expression of CD80 and CD86 on DC in lymph nodes in vivo, with the DDP/LLC group demonstrating more significant results (Figure 4c and Figure S8 (Supporting Information)). Specifically, the expression levels of these costimulatory markers were 3.3-fold higher in the DDP/LLC group than the value of the untreated group. In addition, the number of DC expressing surface markers major histocompatibility complex (MHC) I and MHC II was also notably higher in the DDP/LLC group than in the free LLC lysate protein group,

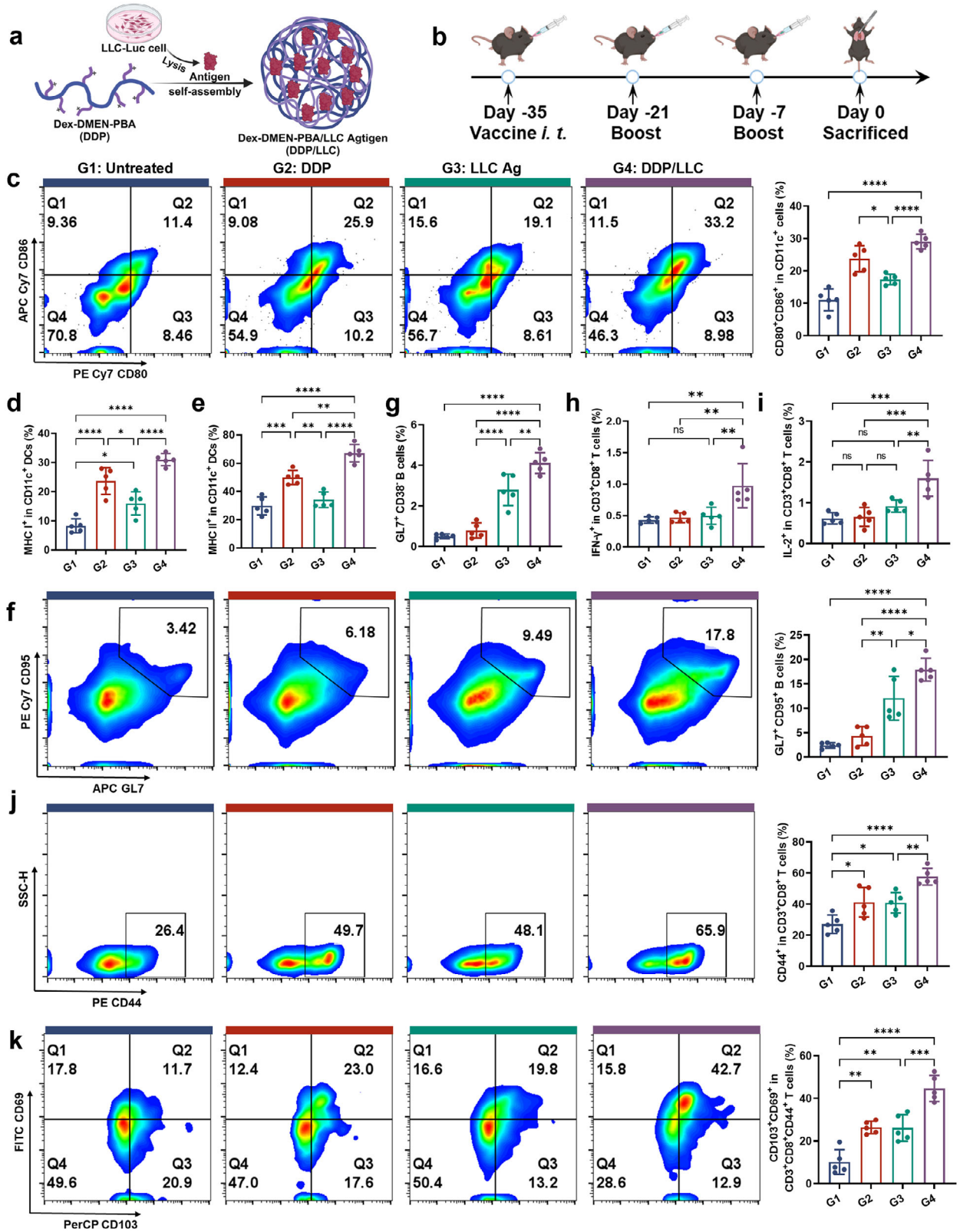

suggesting that DDP/LLC nanovaccine is more effective in promoting DC maturation and enhancing cross-presentation of antigens in vivo (Figure 4d,e and Figure S9 (Supporting Information)). These findings confirmed the superior capacity of DDP in delivering antigen proteins to APCs.

In addition to DC, B cell, well known as effective APCs, also exert a key influence on the immune response.[41–44] The germinal center of the lymph node is the primary site for B cell maturation, where high-affinity antibodies are produced after immunization. Therefore, we also assessed the implication of DDP/LLC on the activation of B cells in the lymph nodes (Figure S10, Supporting Information). Analysis by flow cytometry revealed that the DDP/LLC group significantly increased the activation of germinal center B cells (Figure 4f,g and Figure S11 (Supporting Information)), with an 8.1-fold increase compared to the untreated group and 1.4-fold increase compared to the free antigen group. While free LLC lysate protein also induced some B cells activation, this effect was likely attributed to residual genetic material (e.g., DNA) remaining in the lysed LLC protein.[45] Meanwhile, the function of specific T cells in immune responses was quantified. Mouse spleen T cells were isolated, incubated with LLC lysate protein for 24 h, and analyzed by flow cytometry (Figure S12, Supporting Information). It was found that the expression of IFN-γ in $CD3^+CD8^+$ T cells was 2.0 and 2.3 times higher in the DDP/LLC group compared to the free antigen group and the untreated group, respectively (Figure 4h and Figure S13 (Supporting Information)). Similarly, IL-2 expression in $CD3^+CD8^+$ T cells was significantly elevated in the DDP/LLC group, showing a 1.7-fold increase compared to the free antigen group and 3.3-fold increase compared to the untreated group (Figure 4i and Figure S13 (Supporting Information)). Additionally, TNF-α expression in $CD3^+CD8^+$ T was 1.8-fold elevation than its counterpart in the free antigen group and 2.1-fold increase than in the untreated group (Figure S14, Supporting Information). T_{RM}, which reside indefinitely in tissue, act as the "first line of defense" at barrier locations such as the skin, lungs, and intestinal mucosa.[46,47] $CD8^+$ T_{RM} hold a crucial position in anti-infection and antitumor immunity.[48,49] Therefore, we also assessed the quantity and expression of key surface markers of T_{RM} cells in lung tissue through flow cytometry (Figure S15, Supporting Information). The results demonstrated that all treated groups showed increased expression of CD44 in $CD3^+CD8^+$ T cells within lung tissue to varying degrees, with the DDP/LLC-treated group exhibiting the greatest enhancement (Figure 4j). Moreover, analogous outcomes were witnessed in the manifestation of the T_{RM} cells surface markers CD103 and CD69 (Figure 4k), this result was similar to the reported literature.[50] The increase in their expression of $CD103^+CD69^+$ in $CD3^+CD8^+CD44^+$ T cells was 1.6 times greater than that of free LLC lysate protein group and 4.1 times greater than the untreated group. These findings further validate the substantial advantages of DDP/LLC in preventing tumor occurrence and progression. However, due to limitations in assessing key metrics such as in vivo cross-presentation and antigen-specific T cell proliferation, we utilized the model antigen OVA in parallel experiments to address these challenges. The experimental results revealed that, in comparison to the free OVA group and the DDP group, the DDP/OVA group exhibited a stronger expression of the SIINFEKL-$H2K^{b+}$ peptide and a significant increase in the presence of antigen-specific T cells within lung tissues (Figure S16a,b, Supporting Information). In the evaluation of other metrics in DDP/OVA model, similar results to those in the DDP/LLC model can also be obtained (Figure S17a–j, Supporting Information).

Given the remarkable performance of the DDP/OVA nanovaccine in promoting DC maturation, facilitating antigen cross-presentation, and supporting antigen-specific T cells proliferation in vitro, as well as its ability to potentiate the activation of specific B cells and T cells, we proceeded to evaluate the efficacy of the DDP/LLC nanovaccine in preventing lung tumor growth in vivo. The immunization regimen for mice followed the procedure outlined earlier. One week after the final immunization, mice were challenged with LLC-Luc cells via the tail vein, and tumor growth was monitored at defined intervals by the PerkinElmer IVIS Lumina III. In parallel, the body weight and survival of mice were also tracked. The detailed experimental timeline is shown in **Figure 5**a. As shown in the IVIS imaging results in Figure 5b, no tumor fluorescence signals were detected in any of the mice during the early phase (day 14). However, by days 24 and 28, pronounced tumor fluorescence signals emerged in both the untreated group and the group receiving DDP treatment alone. This development was subsequently accompanied by significant mortality in these groups in the subsequent period (Figure S18, Supporting Information). Although the fluorescence signals in the free LLC lysate protein group and the DDP/LLC group were not notably different in the early phase—likely due to the presence of residual genetic materials within the LLC antigen as discussed earlier—the DDP/LLC nanovaccine group demonstrated superior survival, with survival rates significantly higher than those in the free antigen group. Remarkably, 50% of the LLC-challenged mice in the DDP/LLC nanovaccine remained alive even after six months (Figure 5c). This performance suggests that the assembled DDP/LLC nanovaccine has outstanding prophylactic effects against the invasion of LLC tumor cells. Moreover, no pronounced disparities in body weight were noted throughout the study, indicating the safety of the DDP/LLC nanovaccine (Figure S19, Supporting Information).

Subsequently, peripheral blood was collected from the surviving mice through the orbital venous plexus, and the proportional abundance of memory T cells was measured by flow cytometry.[51] Notably, both effector memory T cells (T_{EM}) and

Figure 4. In vivo immune responses induced by DDP/LLC nanovaccine. a) Schematic diagram illustrating the assembly of DDP/OVA vaccine. b) Detailed timeline of the experimental design used to evaluate the in vivo immune responses triggered by DDP/LLC nanovaccine. c) Representative flow cytometry diagram and the corresponding statistical data (c–e) showing the proportions of $CD80^+CD86^+$, d) MHC I^+, and e) MHC II^+ DC in the thoracic lymph nodes after immunization ($n = 5$). f) Representative diagram and f,g) statistical data showing the proportion of activated germinal center B cells in thoracic lymph nodes after immunization ($n = 5$). Statistical data showing the percentages of h) IFN-γ^+ and i) IL-2^+ in $CD3^+CD8^+$ T cells in restimulated splenocytes ($n = 5$). j,k) Representative diagram and statistical data showing the proportion of j) $CD44^+CD8^+$ T cells and k) the presence of T_{RM} cell markers (CD103, CD69) in the lung after immunization ($n = 5$). Biologically independent mice for each group. Data are presented as the mean ± SD ($n = 5$). Statistical significance was calculated via one-way ANOVA (panels c–k) in GraphPad Prism. * $p < 0.05$, ** $p < 0.01$, *** $p < 0.001$, and **** $p < 0.0001$.

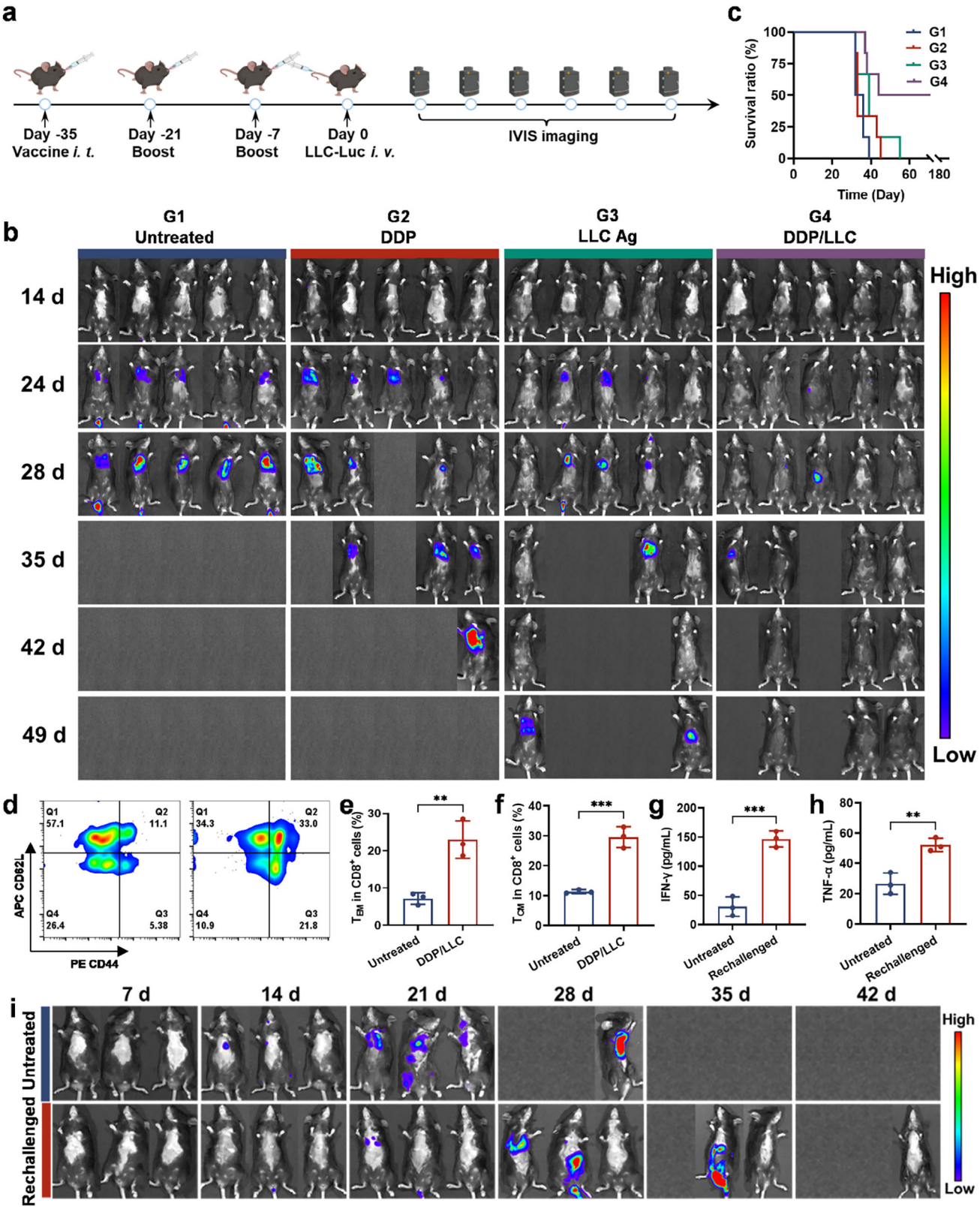

central memory T cells (T_{CM}) in $CD3^+CD8^+$ T cells were significantly increased compared to the control groups (Figure 5d–f). Based on these results, LLC-Luc tumor cells were administered to the surviving mice for rechallenge, and the expression of inflammatory factors in peripheral blood was measured one week after tumor rechallenge. The results showed a marked elevation in IFN-γ and TNF-α values in the rechallenged group relative to the untreated group (Figure 5g,h). Moreover, the tumor growth was continuously monitored by the PerkinElmer IVIS Lumina III imaging system. The imaging results revealed that the untreated mice showed an obvious tumor fluorescence signal after three weeks, while the rechallenged mice showed little or no fluorescence signal (Figure 5i). Approximately one month later, all the mice in the untreated group had died, while the tumor growth in the rechallenged mice was much slower, and they maintained a 33% survival rate, which might be attributed to the elicitation of long-term immune memory (Figure S20, Supporting Information). In summary, these findings strongly suggest that the DDP/LLC nanovaccine offers significant advantages in preventing tumor growth and occurrence. Encouraged by the outstanding performance of the DDP/LLC vaccine, we proceeded to evaluate its potential systemic toxicity. One week after the third immunization (20 μg DDP and 20 μg LLC lysate protein per mouse), blood samples were collected from the mice via the orbital venous plexus for comprehensive hematological and biochemical analyses. Subsequently, the mice were euthanized, and their major organs including heart, liver, spleen, lung and kidney were harvested for hematoxylin and eosin (H&E) staining to thoroughly assess biosafety. Both the hematological analysis and histological H&E staining indicated that DDP/LLC vaccine induced negligible systemic toxicity to mice, even after extended administration (Figure S21a,b, Supporting Information).

2.5. Comparison of Inhalation and Subcutaneous Immunization Strategies

After observing the impressive efficacy of DDP/LLC inhalation vaccine in preventing lung cancer, we were motivated to conduct a comprehensive and unbiased evaluation of the differences and practical value between the inhalation immunization strategies adopted above and the traditional subcutaneous immunization method. As illustrated in **Figure 6a**, mice were vaccinated either subcutaneously or via inhalation with the assembled DDP/LLC nanovaccine, following the same dosage and immune schedule outlined previously. One week after the third immunization, the mice were euthanized, and their thoracic lymph nodes, lungs, and spleens were gathered for immune cell analysis. Germinal center B cells in lymph nodes were a key indicator for comparison. Flow cytometry analysis and representative diagrams revealed that only the inhalation immunization group efficiently activated germinal center B cells populations present in the thoracic lymph nodes (Figure 6b,c), demonstrating a 13.3-fold augmentation relative to the subcutaneous immune group. Although the subcutaneous immunization group activated germinal center B cells in the proximal inguinal lymph nodes, it failed to effectively activate B cells in distal lymph nodes, including the thoracic lymph nodes and other distal sites (Figure S22, Supporting Information). Tfh cells, playing a fundamental and indispensable role in humoral immunity by stimulating the differentiation of germinal center B cells into plasma cells and memory B cells, were also assessed.[52,53] Compared with both the untreated and subcutaneous immunization groups, the inhalation group showed a significant increase in the expression level of programmed death 1 (PD1), inducible T cells costimulator (ICOS), and chemokine receptor (CXCR5)—key proteins positively regulated by Tfh cells (Figure 6d–f and Figure S23 (Supporting Information)). By contrast, the subcutaneous immunization group maintains protein levels equivalent to the untreated group. Interestingly, inhalation immunization not only enhanced the expression of PD1, ICOS, and CXCR5 in Tfh cells within the thoracic lymph nodes but also increased these proteins in the inguinal lymph nodes to some extent (Figure S24, Supporting Information). This distal effect may be attributed to the systemic immune response triggered by inhalation immunity. Similar trends were observed in T_{RM} cells within lung tissue. The inhalation immunization group displayed more remarkable performance than the subcutaneous group in enhancing the expression of CD44 on $CD3^+CD8^+$ T cells within lung tissue (Figure 6g). The inhalation group also showed a more pronounced increase in the expression of the $CD8^+$ T_{RM} cell surface markers CD103 and CD69, displaying a proportional increase of 3.3-fold for the untreated group and 2.4-fold for the subcutaneous group, respectively (Figure 6h). The only minimum difference between the two immunization strategies was observed in the expression of proinflammatory cytokines IFN-γ, IL-2, and TNF-α in the spleen, where both immunization strategies demonstrated nearly identical expression abundances of these cytokines in comparison with the untreated group (Figure 6i–k).

Building on the immune analysis results, we further evaluated the prophylactic effect of each immunization strategy. LLC-Luc tumor cells were injected via the tail vein one week after the third immunization, and tumor growth was monitored using the PerkinElmer IVIS Lumina III system. Imaging results revealed that tumor growth was fastest in the untreated mice, whereas the subcutaneous immunization group effectively delayed tumor progression (Figure S25, Supporting Information). Notably, the inhalation immunization group exhibited superior antitumor effects, with mice displaying weak bioluminescence signals in vivo on day 32, indicating reduced tumor progression (Figure 6l). After the final imaging, the mice were humanely sacrificed, following which their tumors were excised, photographed, and weighed. The in vitro measurements of tumor size and weight were consistent with the in vivo imaging

Figure 5. In vivo prophylactic effects of DDP/LLC nanovaccine. a) Detailed experimental timeline for evaluating the in vivo prophylactic effects in mice using DDP/LLC nanovaccine. b) Bioluminescence imaging of mice following different treatments, monitored from days 17 to 52 ($n = 5$). c) Survival curves of mice bearing LLC-Luc tumors with different treatments ($n = 6$). d) Representative flow cytometry diagram and statistical data of e) T_{EM} and f) T_{CM} in peripheral blood, gated on $CD3^+CD8^+$ T cells, collected on day 180, just before rechallenging with secondary tumors ($n = 3$). Serum levels of g) IFN-γ and h) TNF-α were measured 7 days after rechallenging the mice with LLC-Luc tumors ($n = 3$). i) Bioluminescence imaging of mice post-rechallenged with LLC-Luc tumors ($n = 3$). Biologically independent mice for each group. Data are presented as the mean ± SD ($n = 3$). Statistical significance was calculated via two-sided unpaired *t*-tests (panels e–h) in GraphPad Prism. * $p < 0.05$, ** $p < 0.01$, and *** $p < 0.001$.

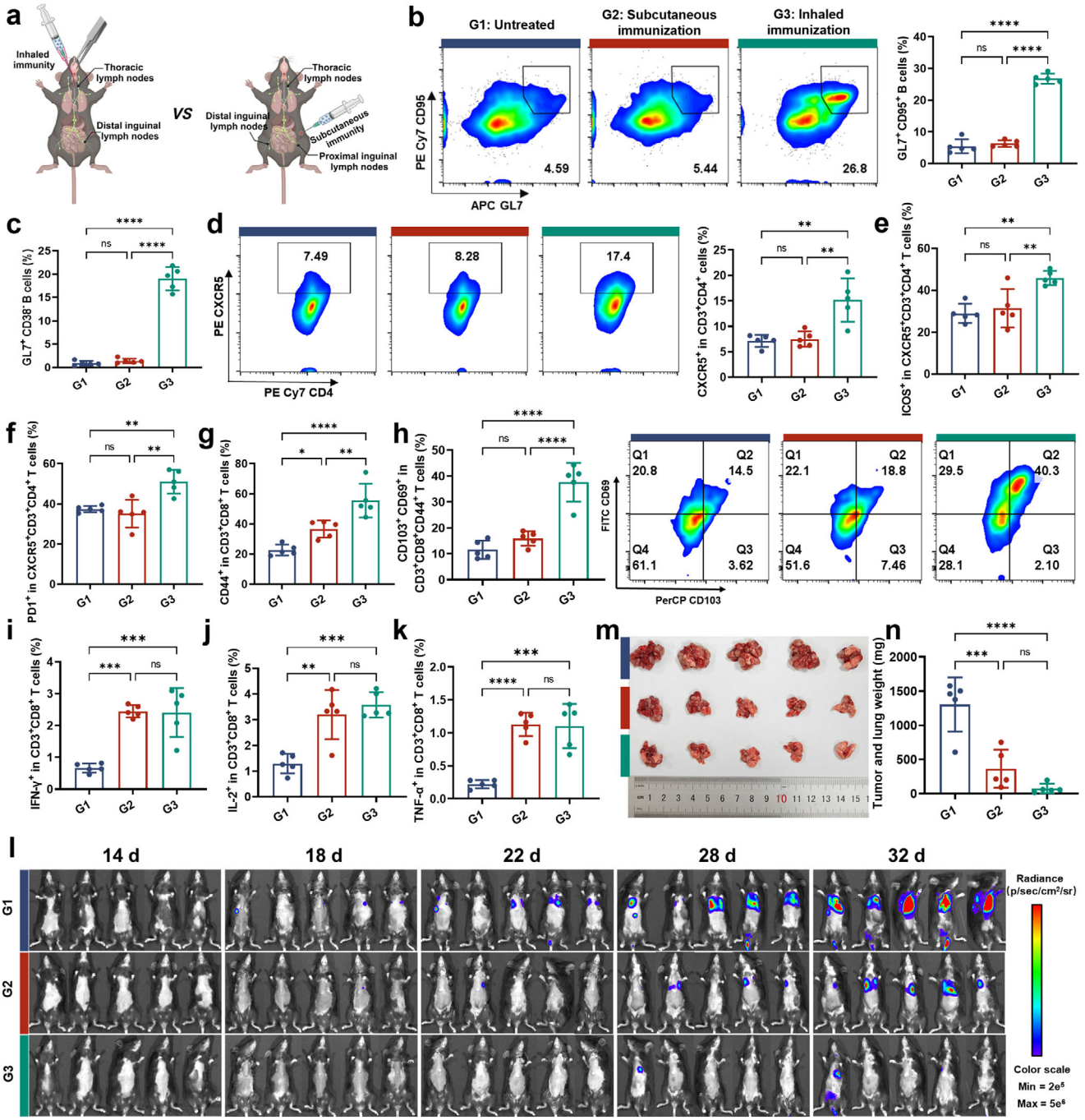

Figure 6. Comparison of in vivo prophylactic effects of DDP/LLC nanovaccine following inhalation and subcutaneous immunization strategies. a) Schematic diagram illustrating the inhalation and subcutaneous immunization strategies. b) Representative diagram and b, c) statistical data showing the proportion of activated germinal center B cells in the thoracic lymph nodes after immunization with different strategies ($n = 5$). d–f) Representative diagram and statistical data showing the proportion of d) $CXCR5^+$, e) $ICOS^+$, and f) $PD1^+$ of Tfh cells after immunization with different strategies ($n = 5$). g,h) Statistical data and representative diagram showing the proportion of g) $CD44^+CD8^+$ T cells and h) $CD103^+CD69^+$ T_{RM} cells in the lung after immunization by different strategies ($n = 5$). i–k) Statistical data showing the proportions of i) IFN-γ^+, j) IL-2^+, and k) TNF-α^+ in $CD3^+CD8^+$ T cells in restimulated splenocytes after immunization with different strategies ($n = 5$). l) Bioluminescence imaging of mice following different immunization strategies from days 14 to 32 ($n = 5$). m,n) Images and tumor weight (including lung) from mice in different groups. Biologically independent mice for each group. Data are presented as the mean ± SD ($n = 5$). Statistical significance was calculated via one-way ANOVA (panels b–k, and n) in GraphPad Prism. * $p < 0.05$, ** $p < 0.01$, *** $p < 0.001$, and **** $p < 0.0001$.

results (Figure 6m,n). The inhalation immunization group exhibited the least tumor growth, confirming the superior efficiency of this approach in inhibiting tumor progression. H&E staining of lung tissue further corroborated these findings. In both the untreated group and the subcutaneous immunization group, a large number of tumor nodules were prominently distributed throughout the lung tissue. By contrast, only a few isolated tumor nodules were observed in the lung tissue of the inhalation immunization group (Figure S26, Supporting Information). These histological results strongly indicate that inhalation immunization offers a more effective strategy for preventing tumor growth compared to subcutaneous immunization. Taken together, these findings provide compelling evidence that inhalation immunization with the DDP/LLC nanovaccine offers superior prophylactic effects against lung tumor growth, both at the immune response level and in terms of long-term tumor suppression. Our research explicates the dormant potential of inhalation immunization as a promising strategy for the development of prophylactic tumor vaccines and their clinical application in cancer prevention.

3. Conclusion

In conclusion, we developed a novel inhalation vaccine carrier DDP based on natural polysaccharide dextran by conjugating with varying degrees of boronic acid substitution. Compared to unmodified dextran and intermediate DD, DDP demonstrated the ability to stimulate BMDC maturation and exhibited optimal adjuvant properties with minimal cytotoxicity when the degree of substitution was 50%. Transcriptomic analysis revealed that DDP induces BMDC maturation by activating multiple inflammatory-associated pathways are involved, such as the cytokine–cytokine receptor interaction, chemokine signaling pathway, TLR signaling pathway, TNF signaling pathway, and the NF-κB signaling pathway. Leveraging the adjuvant properties of this material, DDP could also self-assemble with the antigens including model antigen protein OVA and protein antigens derived from LLC cells to form nanovaccine by electrostatic interaction. Upon inhalation delivery, the DDP/LLC nanovaccine not only effectively activated DC maturation but also significantly enhanced specific T-cell responses and the secretion of inflammatory cytokines, leading to robust antitumor immune responses, along with B-cell activation, providing strong protection against tumor invasion (with 50% cure of mice with LLC tumors). The surviving mice, bolstered by robust immune memory effect, maintained a 33% survival rate even after being rechallenged with LLC tumor cells, underscoring the durability of the immune response elicited by the DDP/LLC nanovaccine. Surprisingly, inhalation immunization demonstrated advantages in preventing lung cancer, likely due to its proximity to the target site and its enhanced ability to activate mucosal immunity. This advantage was reflected not only in the effective activation of B cell maturation in the primary thoracic lymph node but also in the activation of Tfh cells. Moreover, inhalation immunization significantly increased the relative content of T_{RM} in lung tissue, further supporting its superior efficacy. Additionally, the mice in the inhalation delivery group exhibited a better ability to inhibit tumor growth compared to those in the subcutaneous injection group. Overall, our study not only expands the functional application of the natural polysaccharide dextran but also highlights the advantages of inhalation vaccines for lung cancer, particularly through their ability to enhance local immune responses, providing invaluable perspectives conducive to the development of inhalation vaccines and lung-related diseases. Moreover, all materials used in our design are readily available and possess excellent biosafety profiles. The chemical reactions involved are straightforward, requiring no complex catalysis or specialized preparation protocols, supporting the feasibility of scalable manufacturing and ensuring batch-to-batch reproducibility. Collectively, these features underscore the design's significant potential for clinical translation.

4. Experimental Section

Synthesis of DDP: As an example, the synthesis of DDP 100 was carried out by dissolving dextran (200 mg, 1.22 mmol equivalent of sugar units) in ultradry dimethyl sulfoxide (DMSO) (5 mL) at 80 °C under a nitrogen atmosphere. CDI (200 mg, 1.22 mmol) was added to the cold dextran solution to activate the hydroxyl groups, with the reaction allowed to proceed for 2 h at room temperature. DMEN (200 µL, 1.83 mmol) was then added to the activated dextran solution, and the reaction continued for 24 h at room temperature. The mixture was subsequently replaced with *N*,*N*-dimethylformamide, precipitated 3 times with an excess of diethyl ether, and dried under vacuum at 40 °C for 48 h, yielding the yellow product (DD).

PBA (256.8 mg, 1.2 mmol) and glucose (432 mg, 2.4 mmol) were dissolved in anhydrous DMSO and added dropwise to the DD (276 mg) solution in ultradry DMSO under nitrogen atmosphere. The reaction proceeded at 45 °C for 48 h, and then the reaction mixture was dialyzed (MWCO 14 000 Da) against deionized water for 48 h and lyophilized to obtain DDP100.

Preparation and Characterization of DDP/OVA NPs: The DDP/OVA NPs were prepared via a simple and rapid physical mixing method in PBS (pH 7.4). The sizes and zeta potentials of DDP/OVA NPs were measured by the Zetasizer Nano ZS90 (Malvern). The morphology of the nanoparticles was observed using an FEI Tecnai F20 TEM. The loading efficiency of OVA was determined by BCA protein assay kit (Beijing Boxbio Science & Technology Co., Ltd., AKPR017). The secondary structure of the proteins was characterized by CD spectroscopy (JASCO). LLC lysis protein-loaded nanoparticles proceeded similarly.

In Vivo Immune Response Analysis and Antitumor Immunotherapy: To evaluate the prophylactic effect of DDP/antigen vaccine, LLC-Luc cells were lysed using Nonidet P-40, and the resulting antigen protein was mixed with DDP to construct DDP/LLC vaccine. Female C57BL/6 mice were immunized by inhalation method. The specific procedure was as follows: the formulated nanovaccine was loaded into a precision high-pressure nebulization needle. Under mild anesthesia by isoflurane, the nebulization needle was inserted transorally into the trachea of the mice. With controlled pneumatic pressure, the nanovaccine was atomized into an aerosol, delivering it directly to the lower respiratory tract. The mice underwent inhalation immunization on days −35, −21, and −7 with 40 µL of PBS, DDP (20 µg), LLC lysate (20 µg), and DDP/LLC (DDP: 20 µg, LLC: 20 µg). On day 0, each mouse received an intravenous injection of 1×10^6 of LLC-Luc cells. One-week postinjection, the mice were euthanized, and their thoracic lymph node was collected for immune analysis. All animal experiments were performed in compliance with relevant laws and approved by the Institutional Animal Care and Use Committee of Soochow University (No. SUDA20240724A01).

Prophylactic Studies with Inhalational Vaccines: Female C57BL/6 mice (6–8 weeks old) were subjected to inhalational immunization 3 times at two weeks intervals, with each administration consisting of 40 µL PBS, DDP (20 µg), LLC lysate (20 µg), and DDP/LLC (DDP: 20 µg, LLC: 20 µg). 7 days after the final vaccination, the immunized mice were intravenously challenged with 1×10^6 LLC-Luc cells. Tumor growth in the mice was monitored by PerkinElmer IVIS Lumina III imaging system at regular intervals, and the body weight of mice was recorded every 3 days.

Supporting Information

Supporting Information is available from the Wiley Online Library or from the author.

Acknowledgements

Q.Z., Y.M., and Z.C. contributed equally to this work. This article was partially supported by the National Research Programs of China (Grant Nos. 2020YFA0211100, 2022YFA1206500), the National Natural Science Foundation of China (Grant Nos. 52450010, 52325106, 52271248), the program of Shanghai Academic Research Leader (Grant No. 23XD1402900), the Natural Science Foundation of Jiangsu Province (Grant No. BK20240040), the Collaborative Innovation Center of Suzhou Nano Science and Technology, the Suzhou Key Laboratory of Nanotechnology and Biomedicine, and the 111 Program from the Ministry of Education of China.

Conflict of Interest

The authors declare no conflict of interest.

Data Availability Statement

The data that support the findings of this study are available from the corresponding author upon reasonable request.

Keywords

lung cancer, natural polysaccharide, noninvasive nanovaccine, phenylboronic acid

Received: March 13, 2025
Revised: July 15, 2025
Published online:

[1] A. A. Thai, B. J. Solomon, L. V. Sequist, J. F. Gainor, R. S. Heist, L. Cancer, *Lancet* **2021**, *398*, 535.
[2] A. Leiter, R. R. Veluswamy, J. P. Wisnivesky, *Nat. Rev. Clin. Oncol.* **2023**, *20*, 624.
[3] F. Bray, M. Laversanne, H. Sung, J. Ferlay, R. L. Siegel, I. Soerjomataram, A. Jemal, *Ca-Cancer J. Clin.* **2024**, *74*, 229.
[4] G. Mangiameli, U. Cioffi, A. Testori, *Front. Oncol.* **2022**, *12*, 858242.
[5] K. E. Rosenzweig, J. E. Gomez, *J. Clin. Oncol.* **2017**, *35*, 6.
[6] U. Majeed, R. Manochakian, Y. Zhao, Y. Lou, *J. Hematol. Oncol.* **2021**, *14*, 108.
[7] F. Janku, D. J. Stewart, R. Kurzrock, *Nat. Rev. Clin. Oncol.* **2010**, *7*, 401.
[8] J. Liu, X. Li, Y. Li, Q. Gong, K. Luo, *Theranostics* **2025**, *15*, 993.
[9] M. L. Meyer, S. Peters, T. S. Mok, S. Lam, P. C. Yang, C. Aggarwal, J. Brahmer, R. Dziadziuszko, E. Felip, A. Ferris, P. M. Forde, J. Gray, L. Gros, B. Halmos, R. Herbst, P. A. Jänne, B. E. Johnson, K. Kelly, N. B. Leighl, S. Liu, I. Lowy, T. U. Marron, L. Paz-Ares, N. Rizvi, C. M. Rudin, E. Shum, R. Stahel, N. Trunova, P. A. Bunn, F. R., *Ann. Oncol.* **2024**, *35*, 1088.
[10] M.-L. Meyer, B. G. Fitzgerald, L. Paz-Ares, F. Cappuzzo, P. A. Jänne, S. Peters, F. R. Hirsch, *Lancet* **2024**, *404*, 803.
[11] S. Jhunjhunwala, C. Hammer, L. Delamarre, *Nat. Rev. Cancer* **2021**, *21*, 298.
[12] M. J. Lin, J. Svensson-Arvelund, G. S. Lubitz, A. Marabelle, I. Melero, B. D. Brown, J. D. Brody, *Nat. Cancer* **2022**, *3*, 911.
[13] X. Zhou, Y. Wu, Z. Zhu, C. Lu, C. Zhang, L. Zeng, F. Xie, L. Zhang, F. Zhou, *Signal Transduction Targeted Ther.* **2025**, *10*, 7.
[14] J. Holmgren, C. Czerkinsky, *Nat. Med.* **2005**, *11*, S45.
[15] M. Huang, M. Zhang, H. Zhu, X. Du, J. Wang, *Acta Pharm. Sin. B* **2022**, *12*, 3456.
[16] L. Wu, W. Xu, H. Jiang, M. Yang, D. Cun, *Acta Pharm. Sin. B* **2024**, *14*, 5132.
[17] T. Ye, Z. Jiao, X. Li, Z. He, Y. Li, F. Yang, X. Zhao, Y. Wang, W. Huang, M. Qin, Y. Feng, Y. Qiu, W. Yang, L. Hu, Y. Hu, Y. Zhai, E. Wang, D. Yu, S. Wang, H. Yue, Y. Wang, H. Wang, L. Zhu, G. Ma, W. Wei, *Nature* **2023**, *624*, 630.
[18] K. McMahan, F. Wegmann, M. Aid, M. Sciacca, J. Liu, N. P. Hachmann, J. Miller, C. Jacob-Dolan, O. Powers, D. Hope, C. Wu, J. Pereira, T. Murdza, C. R. Mazurek, A. Hoyt, A. C. M. Boon, M. Davis-Gardner, M. S. Suthar, A. J. Martinot, M. Boursiquot, A. Cook, L. Pessaint, M. G. Lewis, H. Andersen, J. Tolboom, J. Serroyen, L. Solforosi, L. M. M. Costes, R. C. Zahn, D. H. Barouch, *Nature* **2023**, *626*, 385.
[19] D. Fu, M. Wang, T. Yang, M. Li, Z. Liang, C. Chen, L. Zhang, C. Xue, B. Sun, C. Mao, *Biomaterials* **2022**, *288*, 121733.
[20] J. Wang, P. Li, Y. Yu, Y. Fu, H. Jiang, M. Lu, Z. Sun, S. Jiang, L. Lu, M. X. Wu, *Science* **2020**, *367*, 869.
[21] F. C. Knight, P. Gilchuk, A. Kumar, K. W. Becker, S. Sevimli, M. E. Jacobson, N. Suryadevara, L. Wang-Bishop, K. L. Boyd, J. E. Crowe, S. Joyce, J. T. Wilson, *ACS Nano* **2019**, *13*, 10939.
[22] T. Sou, E. N. Meeusen, M. de Veer, D. A. V. Morton, L. M. Kaminskas, M. P. McIntosh, *Trends Biotechnol.* **2011**, *29*, 191.
[23] J. Seo, J. Polster, B. Israelow, K. S. Corbett-Helaire, D. R. Martinez, *Nat. Biotechnol.* **2024**, *42*, 1765.
[24] G. A. Roth, V. C. T. M. Picece, B. S. Ou, W. Luo, B. Pulendran, E. A. Appel, *Nat. Rev. Mater.* **2021**, *7*, 174.
[25] B. Eshaghi, A. Schudel, I. Sadeghi, Z. Chen, A. H. Lee, M. Kanelli, F. Tierney, J. Han, B. Ingalls, D. M. Francis, G. Li, U. von Andrian, R. Langer, A. Jaklenec, *Nat. Rev. Mater.* **2023**, *9*, 29.
[26] Q. Hu, Y. Lu, Y. Luo, *Carbohydr. Polym.* **2021**, *264*, 117999.
[27] W. Zhang, M. An, J. Xi, H. Liu, *Bioconjugate Chem.* **2017**, *28*, 1993.
[28] N. Chen, M. M. Johnson, M. A. Collier, M. D. Gallovic, E. M. Bachelder, K. M. Ainslie, *J. Controlled Release* **2018**, *273*, 147.
[29] Y. Gao, W. Wang, Y. Yang, Q. Zhao, C. Yang, X. Jia, Y. Liu, M. Zhou, W. Zeng, X. Huang, S. Chiu, T. Jin, X. Wu, *Adv. Sci.* **2023**, *10*, 2204598.
[30] K. E. Broaders, S. Grandhe, J. M. Frechet, *J. Am. Chem. Soc.* **2011**, *133*, 756.
[31] C. Wang, P. Li, L. Liu, H. Pan, H. Li, L. Cai, Y. Ma, *Biomaterials* **2016**, *79*, 88.
[32] C. Liu, T. Wan, H. Wang, S. Zhang, Y. Ping, Y. Cheng, *Sci. Adv.* **2019**, *5*, aaw8922.
[33] J. Lv, C. Liu, K. Lv, H. Wang, Y. Cheng, *Sci. China Mater.* **2020**, *63*, 620.
[34] H. Zhang, X. Heng, H. Yang, Y. Rao, L. Yao, Z. Zhu, G. Chen, H. Chen, *Angew. Chem., Int. Ed. Engl.* **2024**, *63*, 202402853.
[35] L. Ren, C. Ouyang, S. Zhao, Q. Zheng, W. Guo, B. Fan, J. Zhou, W. Zhang, M. Hu, J. Li, B. Li, *Adv. Healthcare Mater.* **2024**, *13*, 2304575.
[36] Y. Miao, L. Niu, X. Lv, Q. Zhang, Z. Xiao, Z. Ji, L. Chen, Y. Liu, N. Liu, J. Zhu, Y. Yang, Q. Chen, *Adv. Mater.* **2024**, *36*, 2410715.
[37] Z. Cao, L. Ren, L. Niu, R. Zhao, N. Liu, Q. Zhuang, F. Pan, Z. Liu, Y. Cheng, Y. Yang, Q. Chen, *Matter* **2023**, *6*, 3574.
[38] L. Niu, Y. Miao, Z. Cao, T. Wei, J. Zhu, M. Li, B. Bai, L. Chen, N. Liu, F. Pan, J. Zhu, C. Wang, Y. Yang, Q. Chen, *ACS Nano* **2024**, *18*, 3349.
[39] K. M. Peace, T. J. Vreeland, D. F. Hale, D. O. Jackson, J. M. Greene, A. F. Trappey, J. S. Berry, G. T. Clifton, G. S. Herbert, G. Yu, T. Wagner, G. E. Peoples, *J. Clin. Oncol.* **2017**, *35*, 169.
[40] L. Diao, M. Liu, *Adv. Sci.* **2023**, *10*, 2300121.
[41] S. M. Kerfoot, G. Yaari, J. R. Patel, K. L. Johnson, D. G. Gonzalez, S. H. Kleinstein, A. M. Haberman, *Immunity* **2011**, *34*, 947.

[42] M.-I. Yuseff, P. Pierobon, A. Reversat, A.-M. Lennon-Duménil, *Nat. Rev. Immunol.* **2013**, *13*, 475.
[43] S. Hong, Z. Zhang, H. Liu, M. Tian, X. Zhu, Z. Zhang, W. Wang, X. Zhou, F. Zhang, Q. Ge, B. Zhu, H. Tang, Z. Hua, B. Hou, *Immunity* **2018**, *49*, 695.
[44] L. Ren, B. Wang, D. Miao, P. Xiang, Z. Zeng, Z. Li, X. Chen, C. Xu, Q. Gong, K. Luo, J. Jing, *Adv. Mater.* **2025**, *37*, 2417704.
[45] P. Zhang, T. Wang, G. Cui, R. Ye, W. Wan, T. Liu, Y. Zheng, Z. Zhong, *Adv. Mater.* **2024**, *36*, 2407189,.
[46] J. Niessl, T. Sekine, J. Lange, V. Konya, M. Forkel, J. Maric, A. Rao, L. Mazzurana, E. Kokkinou, W. Weigel, S. Llewellyn-Lacey, E. B. Hodcroft, A. C. Karlsson, J. Fehrm, J. Sundman, D. A. Price, J. Mjösberg, D. Friberg, M. Buggert, *Sci. Immunol.* **2021**, *6*, abk0894.
[47] B. S. Sheridan, L. Lefrançois, *Nat. Immunol.* **2011**, *12*, 485.
[48] S. N. Christo, S. L. Park, S. N. Mueller, L. K. Mackay, *Annu. Rev. Immunol.* **2024**, *42*, 317.
[49] E. Menares, F. Gálvez-Cancino, P. Cáceres-Morgado, E. Ghorani, E. López, X. Díaz, J. Saavedra-Almarza, D. A. Figueroae, E. Roa, S. A. Quezada, A. Lladser, *Nat. Commun.* **2019**, *10*, 4401.
[50] K. Rakhra, W. Abraham, C. Wang, K. D. Moynihan, N. Li, N. Donahue, A. D. Baldeon, D. J. Irvine, *Sci. Immunol.* **2021**, *6*, abd8003.
[51] J. Xu, J. Lv, Q. Zhuang, Z. Yang, Z. Cao, L. Xu, P. Pei, C. Wang, H. Wu, Z. Dong, Y. Chao, C. Wang, K. Yang, R. Peng, Y. Cheng, Z. Liu, *Nat. Nanotechnol.* **2020**, *15*, 1043.
[52] C. Cui, J. Wang, E. Fagerberg, P. M. Chen, K. A. Connolly, M. Damo, J. F. Cheung, T. Mao, A. S. Askari, S. Chen, B. Fitzgerald, G. G. Foster, S. C. Eisenbarth, H. Zhao, J. Craft, N. S. Joshi, *Cell* **2021**, *184*, 6101.
[53] S. A. Schattgen, J. S. Turner, M. A. Ghonim, J. C. Crawford, A. J. Schmitz, H. Kim, J. Q. Zhou, W. Awad, R. C. Mettelman, W. Kim, K. M. McIntire, A. Haile, M. K. Klebert, T. Suessen, W. D. Middleton, S. A. Teefey, R. M. Presti, A. H. Ellebedy, P. G. Thomas, *Nat. Immunol.* **2024**, *25*, 1742.

Supporting information

A Non-Invasive and Highly Effective Inhaled Nanovaccine Based on Natural Polysaccharide for Lung Cancer Treatment

Qiang Zhang, Yu Miao, Zhike Chen, Yi Liu, Linfu Chen, Zhisheng Xiao, Hui Shen, Jingjing Shen, Feng Pan, Nanhui Liu, Xinying Lv, Haibin Zhao, Qifan Yu, Zixuan Zheng, Qian Chen, Yang Yang**

Q. Zhang, Y. Liu, F. Pan, Q. Yu, Z. Zheng, Y. Yang
Department of Thoracic Surgery, Shanghai Pulmonary Hospital, School of Medicine, Tongji University, Shanghai, 200433, China.
E-mail: timyangsh@tongji.edu.cn.

Q. Zhang, Y. Yang
School of Materials Science and Engineering, Tongji University, Shanghai, 201804, China.
E-mail: timyangsh@tongji.edu.cn.

Y. Yang
Innovation and Incubation Center, Shanghai Pulmonary Hospital, School of Medicine, Tongji University, Shanghai 200433, China.
E-mail: timyangsh@tongji.edu.cn.

Q. Zhang, Y. Miao, Z. Chen, L. Chen, Z. Xiao, H. Shen, J. Shen, N. Liu, X. Lv, H. Zhao, Q. Chen
Institute of Functional Nano & Soft Materials (FUNSOM), Jiangsu Key Laboratory for CarbonBased Functional Materials & Devices, Soochow University, Suzhou, 215123, China.
E-mail: chenqian@suda.edu.cn

Z. Chen
Department of Thoracic Surgery, The First Affiliated Hospital of Soochow University, Suzhou, 215006, China.

H. Shen
Department of Thoracic Surgery, Shanghai General Hospital, Shanghai Jiao Tong University School of Medicine, Shanghai, 200086, China.

Materials and methods

Materials, cells, and animals

Dextran (Dex, >98%, Shanghai Aladdin Biochemical Technology Co., Ltd.), *N, N*-Dimethylethylenediamine (DMEN, >98%, Shanghai Aladdin Biochemical Technology Co., Ltd.), 4-(Bromomethyl)phenylboronic acid (PBA, ≥99%, Beijing Mreda Technology Co., Ltd.), Carbonyldiimidazole (CDI, ≥98%, Adamas-beta®, Shanghai Titan Scientific Co., Ltd) were purchased for use in the synthesis. 3-(4,5-Dimethylthiazol-2-yl)-2,5-diphenyltetrazoliumbromide (MTT) and Lipopolysaccharide (LPS) were purchased from Sigma-Aldrich. Reagents not specifically mentioned were sourced from Sinopharm Chemical Reagent Co., Ltd. and used without further purification.

DC2.4 cells were cultured in Roswell Park Memorial Institute (RPMI) 1640 medium supplemented with 10% fetal bovine serum (FBS) (Inner Mongolia Jin Yuan Kang Biotechnology Co., Ltd., JYK-FBS-301) and 1% penicillin-streptomycin (Pricella Life Science & Technology Co., Ltd., PB180120) at 37 ℃ in 5% CO_2. LLC-Luc cells were cultured in DMEM with high glucose containing 10% FBS and 1% penicillin-streptomycin at 37 ℃ in 5% CO_2. Female C57BL/6 mice (6-8 weeks) were purchased from Changzhou Cavens Experimental Animal Co., Ltd. All animal experiments were performed in compliance with relevant laws and approved by the Institutional Animal Care and Use Committee of Soochow University (No. SUDA20240724A01).

Characterization

Nuclear magnetic resonance (NMR) spectra were recorded at room temperature using a Unity Inova 400 spectrometer. DMSO-d_6 (J&K Scientific, D615712), D_2O (Macklin Biochemical, D807644) or their mixture was used as solvents. The progress of polymer reactions was monitored by Fourier transform infrared (FT-IR) spectroscopy using a Nicolet 6700 spectrometer. The size distribution and zeta potential of nanoparticles were determined using a Malvern Zetasizer Nano ZS.

Synthesis of DDP

As an example, the synthesis of DDP 100 was carried out by dissolving dextran (200 mg, 1.22 mmol equivalent of sugar units) in ultradry DMSO (5 mL) at 80 ℃ under a nitrogen atmosphere. 1,1'-Carbonyldiimidazole (CDI, 200 mg, 1.22 mmol) was added to the cold dextran solution to activate the hydroxyl groups, with the reaction allowed to proceed for 2 hours at room temperature. *N*, *N*-Dimethylethylenediamine (DMEN, 200 μL, 1.83 mmol) was then added to the activated dextran

solution, and the reaction continued for 24 hours at room temperature. The mixture was subsequently replaced with DMF, precipitated three times with an excess of diethyl ether, and dried under vacuum at 40 ℃ for 48 hours, yielding the yellow product (Dex-DMEN). Yield: 92%. The ^{1}H NMR (400 MHz, DMSO-d_6) showed the following peaks: δ 5.20-4.83 and 4.14-3.42 (Dextran), 2.89 (-NHCH_2CH$_2$-), 2.73 (-CH$_2$CH_2N-), 2.24 (-N(CH_3)$_2$).

4-(Bromomethyl)phenylboronic acid (PBA, 256.8 mg, 1.2 mmol) and glucose (432 mg, 2.4 mmol) were dissolved in anhydrous DMSO and added dropwise to the Dex-DMEN (276 mg) solution in ultradry DMSO under nitrogen atmosphere. The reaction proceeded at 45 ℃ for 48 h, and then the reaction mixture was dialyzed (MWCO 14000 Da) against deionized water for 48 hours and lyophilized to obtain Dex-DMEN-PBA (DDP100). Yield: 78%. The ^{1}H NMR (400 MHz, D$_2$O) revealed the following chemical shifts: δ 7.86 and 7.57 (-C$_6H_4$B(OH)$_2$), 5.20-4.83 and 4.14-3.42 (Dextran), 3.11 (-N(CH_3)$_2$), 2.91 (-NHCH_2CH$_2$-), 2.71 (-CH$_2$CH_2N-). The Dex-DMEN-PBA with different modification ratios can be obtained by adjusting the feed of DMEN and PBA.

Preparation and characterization of DDP/OVA NPs

The DDP/OVA NPs were prepared via a simple and rapid physical mixing method in PBS (pH 7.4). The sizes and zeta potentials of DDP/OVA NPs were measured by the Zetasizer Nano ZS90 (Malvern). The morphology of the nanoparticles was observed using an FEI Tecnai F20 transmission electron microscope (TEM). The loading efficiency of OVA was determined by bicinchoninic acid (BCA) protein assay kit (Beijing Boxbio Science & Technology Co., Ltd., AKPR017). The secondary structure of the proteins was characterized by circular dichroism (CD) spectroscopy (JASCO). LLC lysis protein-loaded nanoparticles proceeded similarly.

Cellular uptake and endocytic pathway

DC2.4 cells were cultured in 24-well plates at a density of 3 × 10^5 cells per well and incubated overnight. Subsequently, different formulations including Free OVA-FITC (20 μg mL^{-1}), and DDP/OVA-FITC (DDP: 20 μg mL^{-1}, OVA: 20 μg mL^{-1}) were added. Following 4 hours incubation, the cells were collected and analyzed by flow cytometry (FongCyte™).

For the internalization assay, DC2.4 cells were seeded into confocal glass dishes (NEST Biotechnology, 801001) suitable for confocal laser scanning microscopy (CLSM) and incubated with Free OVA-FITC and DDP/OVA-FITC (DDP: 20 μg mL^{-1}, OVA: 20 μg mL^{-1}) for 1 and 2 hours. Then, the cells were washed three times with PBS, stained with DAPI (7.5 μg mL^{-1}, 10 min) and LysoTracker

Red (100 nM, 1 h), and imaged using confocal laser scanning microscopy (CLSM, ZEISS LSM 800 with Airyscan).

To investigate the endocytic pathways of DDP/OVA-FITC NPs, DC2.4 cells were pretreated with different inhibitors (AMZ, 100 μM; Geni, 150 μM; CPZ, 15 μM; MβCD, 2 mM) for 2 h and then incubated with DDP/OVA-FITC NPs at 37°C for 4 h. As a control, DC2.4 cells were pretreated at 4°C for 2 hours and then incubated with DDP/OVA-FITC NPs at 4°C for 4 h.

DC maturation and cross-presentation *in vitro*

Bone-marrow-derived dendritic cells (BMDCs) were isolated from C57BL/6 mouse bone marrow, and cultured in the complete DC medium containing 10% FBS, 1% penicillin-streptomycin, 55 μM β-mercaptoethanol (Gibco, 2466010), 20 ng mL^{-1} granulocyte-macrophage colony stimulating factor (GM-CSF, Novoprotein, Shanghai, China, CK02), and 10 ng mL^{-1} Interleukin-4 (IL-4, HUABIO, HA210902) at 37℃ with 5% CO_2. To evaluate the ability of DDP to stimulate BMDC maturation, BMDCs were incubated with free OVA (20 μg mL^{-1}), DDP (20 μg mL^{-1}) and DDP/OVA (DDP: 20 μg mL^{-1}, OVA: 20 μg mL^{-1}) for 24 hours. The supernatants were harvested and analyzed for cytokine levels (TNF-α (Beijing Solarbio Science & Technology Co., Ltd., SEKM-0034), IL-6 (Jianglai, JL20268) and IL-1β (Beijing Solarbio Science & Technology Co., Ltd., SEKM-0002) using enzyme-linked immunosorbent assay (ELISA). Additionally, the cells were collected, resuspended in PBS containing 1% FBS, and incubated with anti-CD16/32 (BioLegend, 101303) at room temperature. The cells were then stained with anti-CD11c-FITC (BioLegend, 117306), anti-CD80-PE (BioLegend, 104708), and anti-CD86-APC (BioLegend, 159216) for flow cytometry analysis. To measure cross-presentation, BMDCs treated with different formulations for 24 hours were collected, resuspended in PBS containing 1% FBS, and stained with anti-CD16/32. The cells were then incubated with anti-CD11c-FITC and anti-SIINFEKL-H2K^b-APC (BioLegend, 141606) for flow cytometry analysis.

$CD8^+$ T cell priming assay *in vitro*

BMDCs were incubated with free OVA (20 μg mL^{-1}), DDP (20 μg mL^{-1}), or DDP/OVA (DDP: 20 μg mL^{-1}, OVA: 20 μg mL^{-1}) at 37 ℃ for 24 hours, followed by washing with PBS containing 0.1% BSA. Spleen cells isolated from OT-I mice were stained with the CellTrace CFSE Cell Proliferation Kit according to the vendor's instructions. The treated BMDCs (1×10^5 cells mL^{-1}) were co-cultured with CFSE-stained splenic T cells in round-bottom 96-well plates for 72 hours. Following incubation, the cells were collected, washed with PBS containing 0.1% BSA, blocked with anti-CD16/32 at room

temperature, and subsequently stained with anti-CD3-APC (BioLegend, 100236) and anti-CD8a-PE (BioLegend, 141604) for flow cytometry.

RNA transcriptomic analysis

To investigate the molecular mechanisms underlying BMDCs maturation induced by DDP, BMDCs were incubated with DDP for 24 hours and subsequently collected for RNA-sequencing analysis using Lc-bio Technologies. The RNA-seq data were processed using the bioinformatics software provided by Lc-bio Technologies for quality control and analysis. For quantitative PCR (qPCR) validation, total RNA was extracted from the treated cells using TRIzol reagent, as per the manufacturer's protocol. cDNA synthesis and subsequent qPCR were performed using the BeyoFast SYBR Green One-Step qRT-PCR Kit (Beyotime, China), following the manufacturer's instructions in the Bioland™ PCR strip tubes (Bioland Biotechnology Co. Ltd). PCR amplification was carried out using an Agilent Technologies Stratagene Mx3005P Real-Time PCR System. The following primers were used. IL6 forward: CGGCCTTCCCTACTTCACAA, IL6 reverse: TTCTGCAAGTGCATCATCGT, CD80 forward: CTTTCAGACCGGGGCACATA, CD80 reverse: GTGTCTGCAGATGGGTTTCC, TNFSF9 forward: TGTTCCTATCTTCACCCGCA, TNFSF9 reverse: GGAGAGCCCTGTTGTGTAGT, CCL22 forward: GCTCTCGTCCTTCTTGCTGT, CCL22 reverse: GCAGAGGGTGACGGATGTAG. Relative RNA expression levels were normalized to GAPDH expression and the corresponding levels in the untreated control sample.

***In vivo* immune response analysis and antitumor immunotherapy**

To evaluate the prophylactic effect of DDP/antigen vaccine, LLC-Luc cells were lysed using Nonidet P-40 (NP-40), and the resulting antigen protein was mixed with DDP to construct DDP/LLC vaccine. Female C57BL/6 mice were immunized by inhalation method. The specific procedure was as follows: The formulated nanovaccine was loaded into a precision high-pressure nebulization needle. Under mild anesthesia by isoflurane, the nebulization needle was inserted transorally into the trachea of the mice. With controlled pneumatic pressure, the nanovaccine was atomized into an aerosol, delivering it directly to the lower respiratory tract. The mice underwent inhaled immunization on days -35, -21 and -7 with 40 μL of PBS, DDP (20 μg), LLC lysate (20 μg), and DDP/LLC (DDP: 20 μg, LLC: 20 μg). On day 0, each mouse received an intravenous injection of 1×10^6 of LLC-Luc cells. One-week post-injection, the mice were euthanized, and their thoracic lymph node was collected. The lymph nodes were mechanically disrupted to generate a single-cell suspension in PBS/1%FBS (KX-

A1221, Inner Mongolia Wanrui Biotechnology Co., Ltd). A portion of this suspension was used to assess DC maturation. Specifically, cells were blocked with anti-CD16/32 to avoid non-specific binding and subsequently stained with anti-CD11c-FITC, anti-CD80-PE Cy7 (BioLegend, 104734), anti-CD86-APC Cy7 (BioLegend, 105030), anti-MHC I-APC (BioLegend, 114714), and anti-MHC II-PE (BioLegend, 116408) for flow cytometry analysis. To access the activation of B cells, the lymph node cells were blocked with anti-CD16/32 and stained with anti-GL7-APC (BioLegend, 144618), anti-B220-PE (BioLegend, 103208), anti-CD95-PE Cy7 (BioLegend, 152618), and anti-CD38-FITC (BioLegend, 165608) for flow cytometry analysis.

For the analysis of tissue-resident memory T cells in the lung, the lungs were collected and mechanically dissociated into single-cell suspension. The cells were then blocked with anti-CD16/32 and stained with anti-CD3-APC, anti-CD8-APC Cy7 (BioLegend, 100714), anti-CD4 PE Cy7 (BioLegend, 100422), anti-CD44 PE (BioLegend, 103024), anti-CD69-FITC (BioLegend, 104506) and anti-CD103 PerCP (BioLegend, 121416) for flow cytometry analysis. To examine the presence of antigen-specific T cells in the spleen, splenocytes were splenocytes were isolated, subjected to erythrocyte lysis (ZUNYAN, NanJing, China, ZYFB006-0100), and subsequently blocked and stained with anti-CD3-FITC (BioLegend, 100204), anti-CD8-PerCP (BioLegend, 104014), anti-CD4 APC Cy7 (BioLegend, 100414), anti-IFN-γ PE (BioLegend, 505808), anti-IL2-APC (BioLegend, 503810) and anti-TNF-α PE Cy7 (BioLegend, 506323) for flow cytometry analysis.

In addition, we utilized OVA as the model antigen to further assess the expression of SIINFEKL $H2K^{b+}$ peptide in the thymic lymph nodes and the relative abundance of antigen-specific T cells in lung tissues. The lymph single-cell suspensions were then blocked with anti-CD16/32 and stained with anti-CD11c-FITC, anti-CD80-PE Cy7, anti-CD86-APC Cy7 and APC-anti-H-$2K^{b}$ bound to SIINFEKL (BioLegend, 141606) for flow cytometry analysis. Anti-CD8 PE Cy7 and PE-labeled SIINFEKLMHC class I tetramer for flow cytometry analysis.

Prophylactic studies with inhalational vaccines

Female C57BL/6 mice (6-8 weeks old) were subjected to inhaled immunization three times at two-week intervals, with each administration consisting of 40 μL PBS, DDP (20 μg), LLC lysate (20 μg), and DDP/LLC (DDP: 20 μg, LLC: 20 μg). 7 days after the final vaccination, the immunized mice were intravenously challenged with 1×10^6 LLC-Luc cells. Tumor growth in the mice was monitored by PerkinElmer IVIS® Lumina III imaging system at regular intervals, and the body weight of mice

was recorded every three days.

Immunological memory responses triggered by DDP/LLC vaccine

For the analysis of memory T cells, circulating peripheral blood mononuclear cells from the peripheral blood were harvested from the surviving mice and stained with anti-CD3-FITC, anti-CD8-PerCP, anti-CD62L-APC (BioLegend, 161217) and anti-CD44-PE for flow cytometry analysis. The surviving mice were rechallenged with LLC-Luc cells again to assess the effect of preventing tumor growth. One week after tumor rechallenge, the expression of cytokines of TNF-α and IFN-γ in peripheral blood was collected and measured by ELISA kit (absin, abs520010, abs520007). Tumor growth in the mice was monitored by PerkinElmer IVIS® Lumina III imaging system at regular intervals.

Statistical analysis

Data are presented as the mean ± Standard Deviation (SD) unless otherwise indicated in the figure captions. Statistical significance was determined using ordinary one-way ANOVA for comparisons involving more than two groups, and unpaired t-test for two-group comparisons. All statistical analyses were performed using GraphPad Prism software (Prism 9.0) or Microsoft Excel 2019. Survival curves were obtained using the Kaplan-Meier method and compared by the log-rank test. The threshold for statistical significance was *$p < 0.05$, **$p < 0.01$, ***$p < 0.001$, and ****$p < 0.0001$.

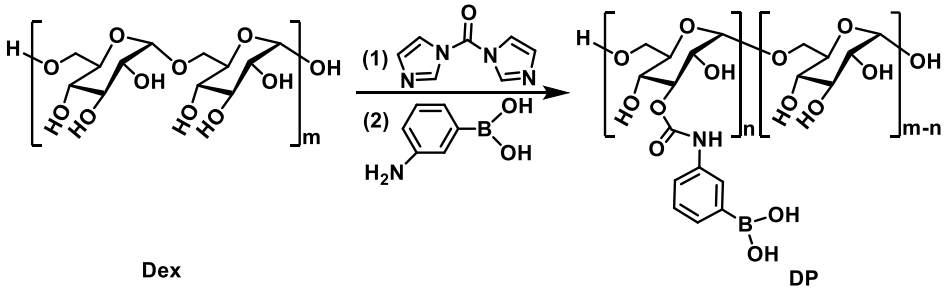

Figure S1. Synthesis route of phenylboronic acid-conjugated dextran (Dex-PBA, DP). Conditions: (1) Dextran, CDI, DMSO, R.T., 2 h; (2) 3-aminobenzeneboronic acid, R.T., 24 h.

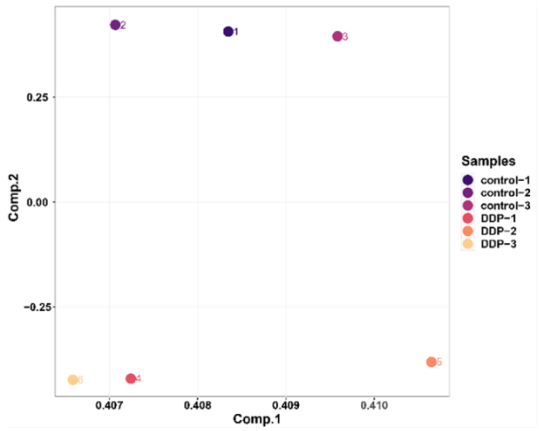

Figure S2. Principal component analysis (PCA) showed the distribution of samples in the control and DDP groups.

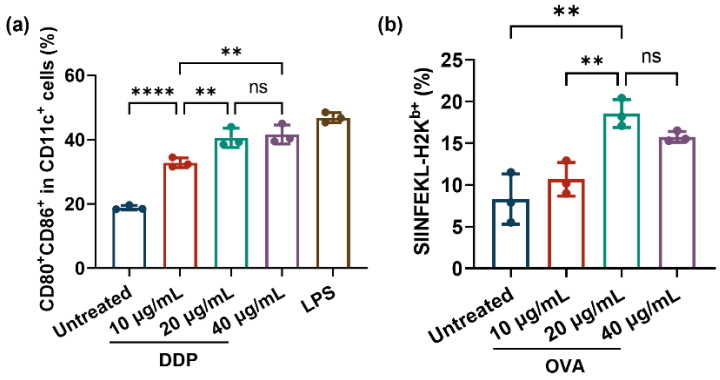

Figure S3. Statistical data showing the percentages of $CD86^{+}CD80^{+}$ BMDCs (A) and SIINFEKL-$H2K^{b+}$ presenting BMDCs (B) after different treatments (n = 3).

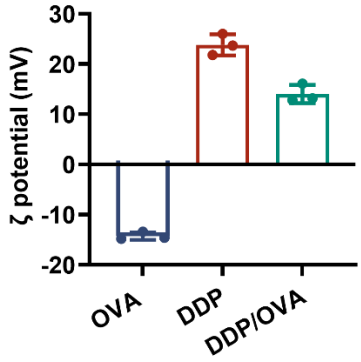

Figure S4. The zeta potential of free OVA, DDP and DDP/OVA. Data are presented as the mean ± SD (n = 3).

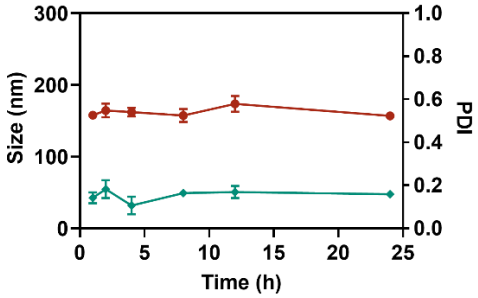

Figure S5. The stability of DDP/OVA in PBS at different time points (n = 3).

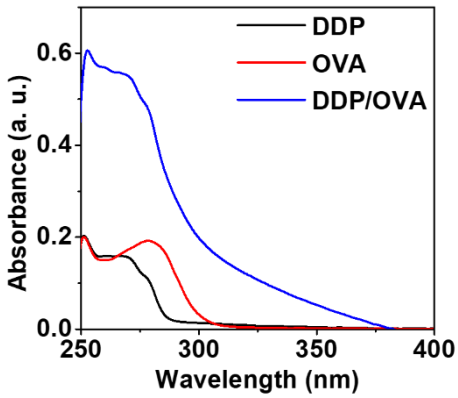

Figure S6. The UV-visible absorbance spectra of free OVA, DDP and DDP/OVA.

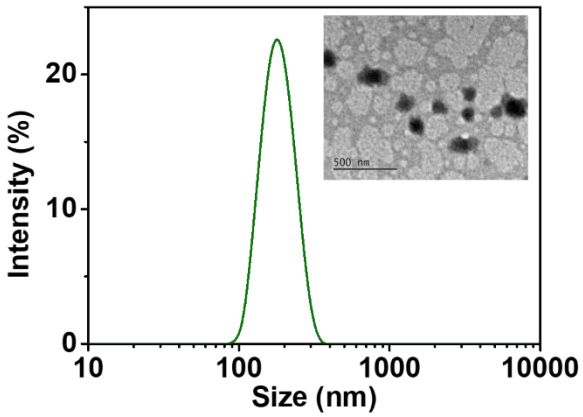

Figure S7. Size distribution of assembled DDP/LLC vaccine, with an inset showing a TEM image.

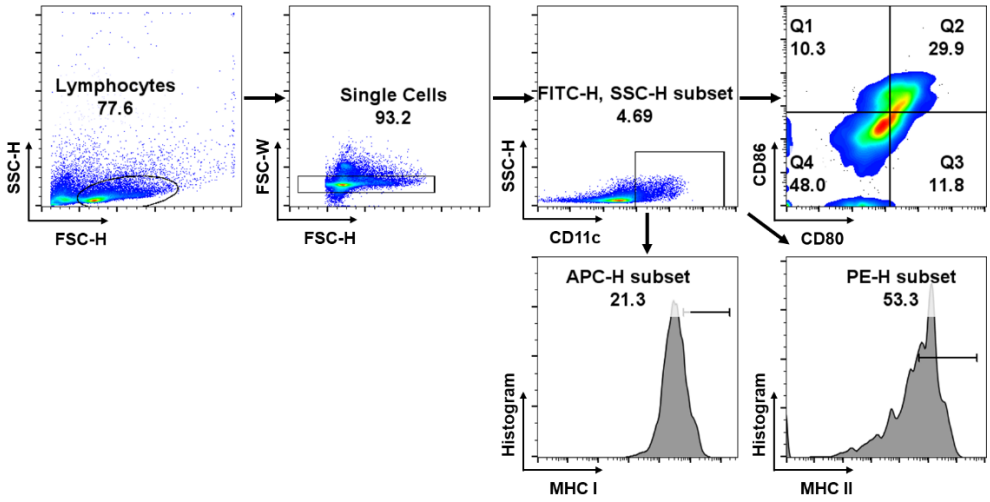

Figure S8. Flow cytometry gating strategy for the analysis of DCs maturation, and cross-presentation in vivo.

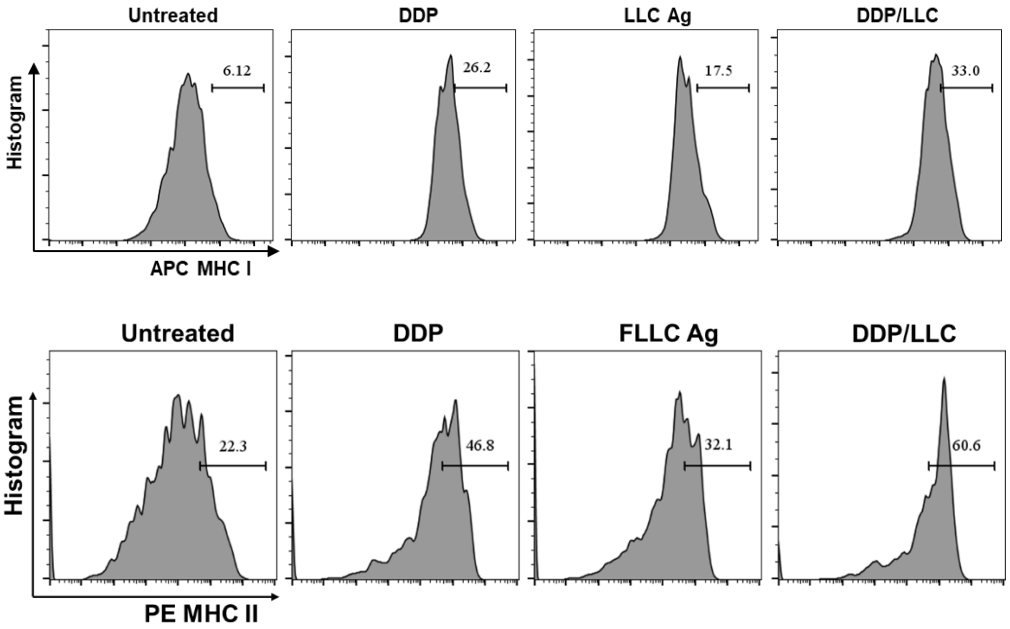

Figure S9. Representative flow cytometry diagram showing the proportions of MHC I^+ and MHC II^+ DCs in the thoracic lymph nodes after immunization.

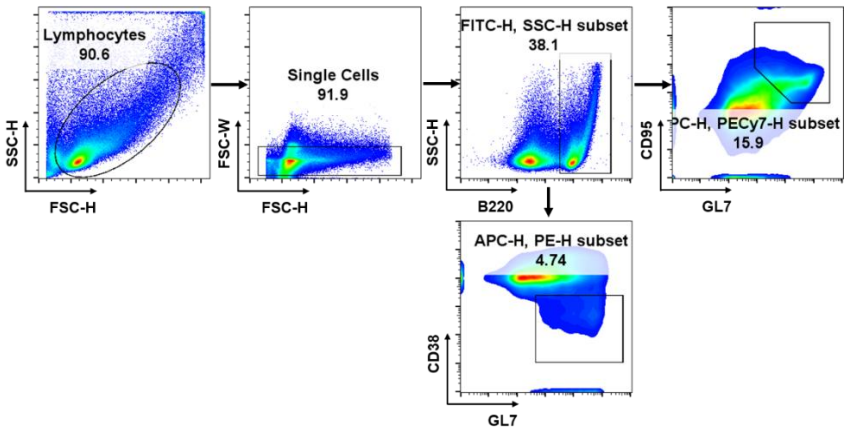

Figure S10. Flow cytometry gating strategy for the analysis of germinal center B cells activation.

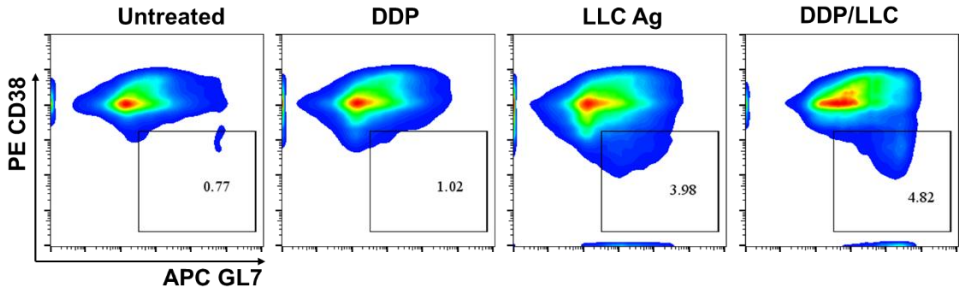

Figure S11. Representative flow cytometry diagram showing the proportions of germinal center B cells activation in the thoracic lymph nodes after immunization.

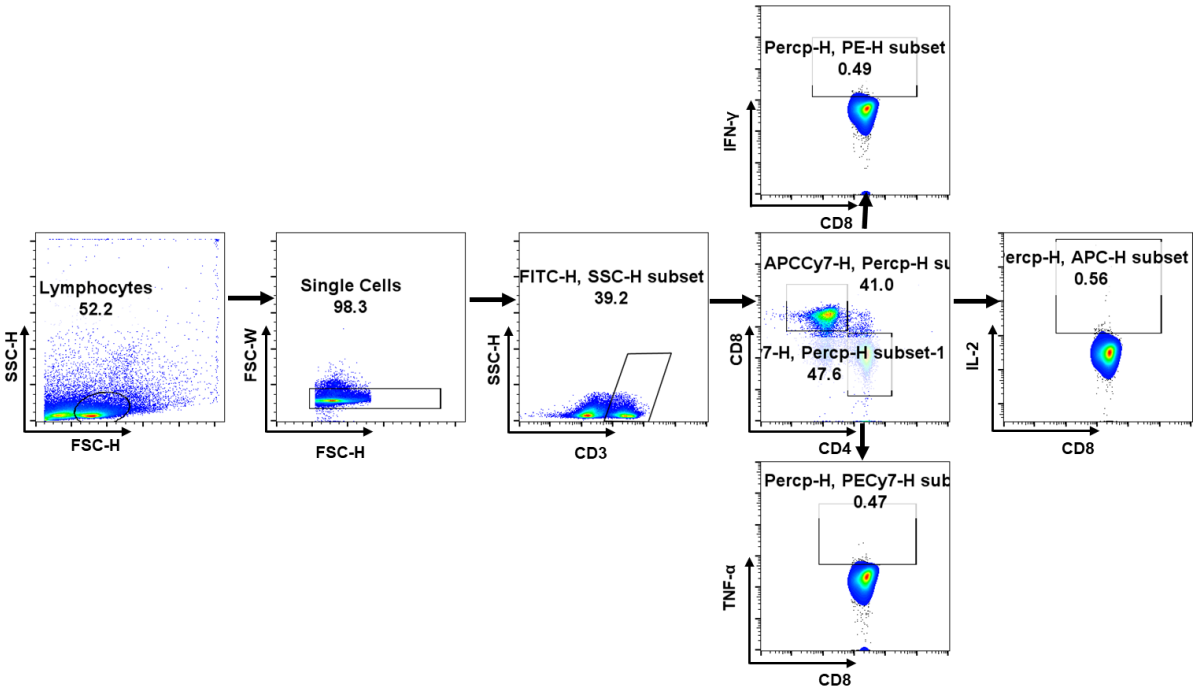

Figure S12. Flow cytometry gating strategy for the analysis of spleen T cells after immunization.

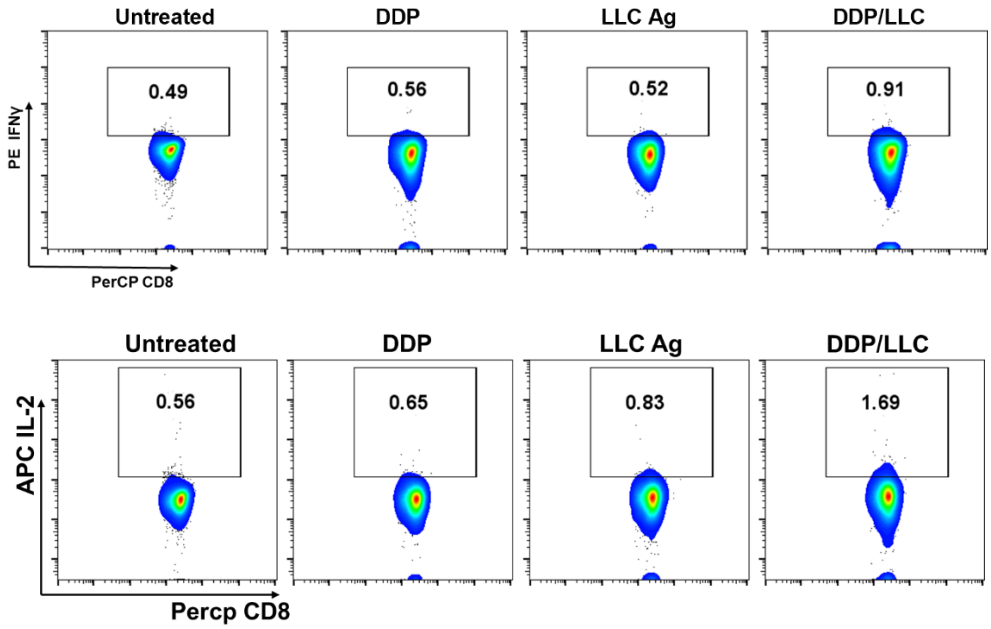

Figure S13. Representative flow cytometry diagram showing the proportions of IFN-γ^+ and IL-2^+ in $CD3^+CD8^+$ T cells in restimulated splenocytes.

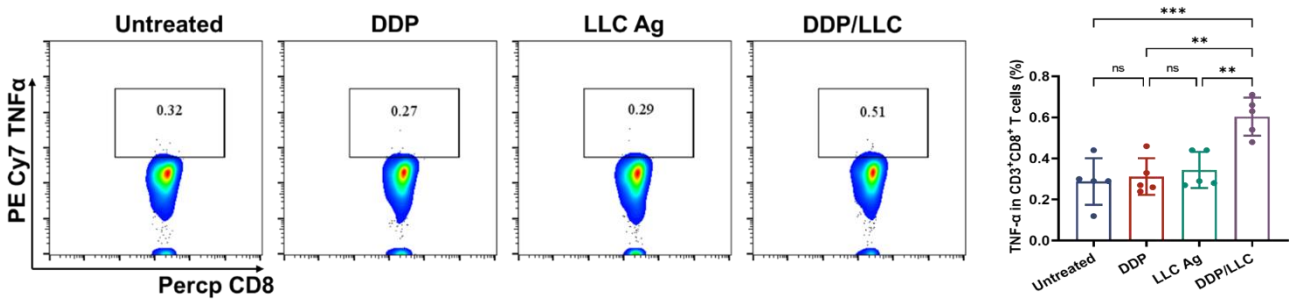

Figure S14. Representative flow cytometry diagram and and corresponding statistical data showing the proportions of TNF-α^+ in $CD3^+CD8^+$ T cells in restimulated splenocytes. Data are presented as the mean ± SD (n = 5). Statistical significance was calculated via one-way ANOVA in GraphPad Prism. * $p < 0.05$, ** $p < 0.01$, *** $p < 0.001$, and **** $p < 0.0001$.

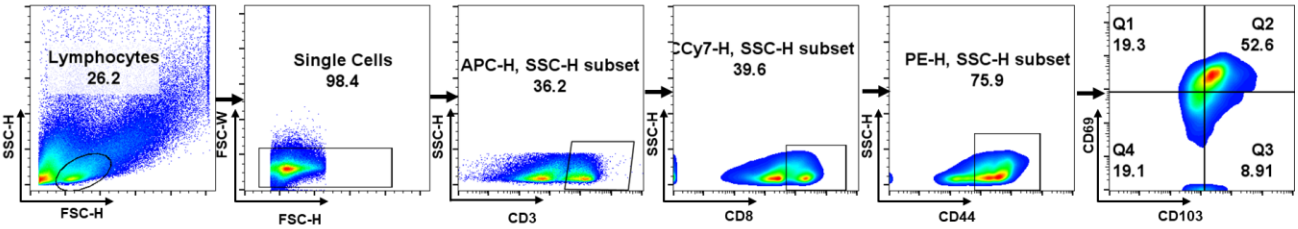

Figure S15. Flow cytometry gating strategy for the analysis of resident T cells in lung tissue.

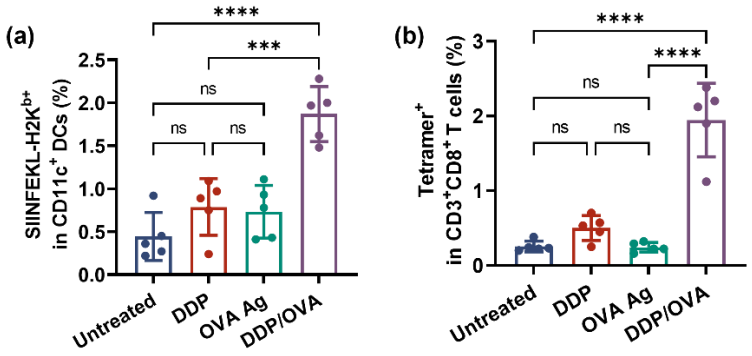

Figure S16. Statistical data showed the proliferation of antigen cross-presentation (SIINFEKL-$H2K^{b+}$) in DCs in thoracic lymph nodes (a) and the proportion of $H2K^{b+}$/SIINFEKL $Tetramer^+CD3^+CD8^+$ T cells in spleen T cells (b) after immunization. Data are presented as the mean ± SD (n = 5). Statistical significance was calculated via one-way ANOVA in GraphPad Prism. * $p < 0.05$, ** $p < 0.01$, *** $p < 0.001$, and **** $p < 0.0001$.

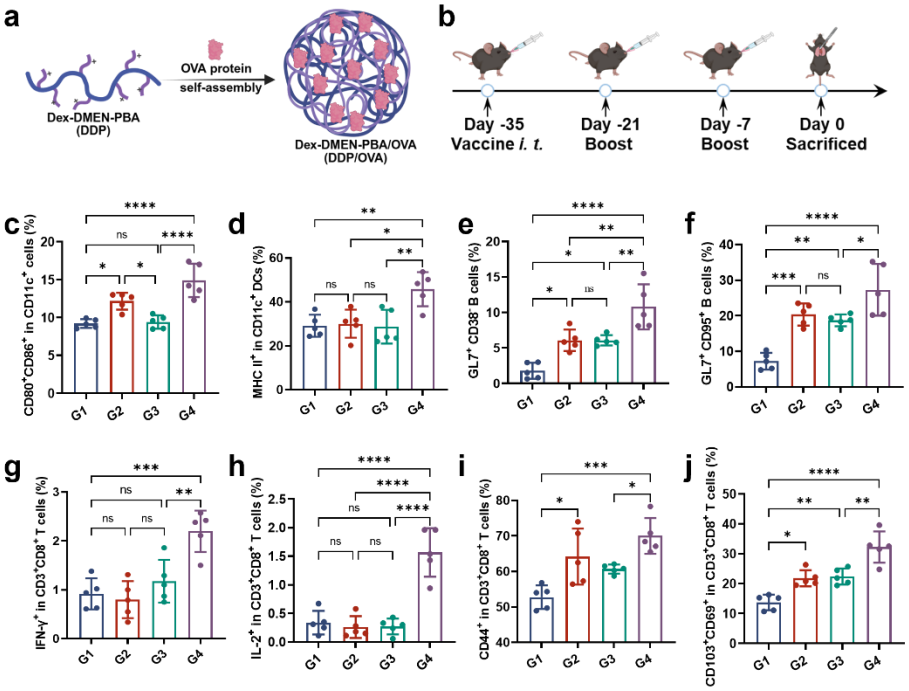

Figure S17. In vivo immune responses induced by DDP/OVA nanovaccine. (a) Schematic diagram illustrating the assembly of DDP/OVA vaccine. (b) Detailed timeline of the experimental design used to evaluate the in vivo immune responses triggered by DDP/OVA nanovaccine. (c-d) Statistical data showing the proportions of $CD80^+CD86^+$ DCs (c) and MHC II^+ DCs (d) in the thoracic lymph nodes after immunization (n = 5). (e-f) Statistical data showing the proportion of activated germinal center B cells in thoracic lymph nodes after immunization (n = 5). (g-h) Statistical data showing the percentages of IFN-γ^+ and IL-2^+ in $CD3^+CD8^+$ T cells in restimulated splenocytes (n = 5). (i-j) Statistical data showing the proportion of $CD44^+CD8^+$ T cells (i) and the presence of tissue-resident T cell markers (CD103, CD69) (j) in the lung after immunization (n = 5). Biologically independent mice for each group. Data are presented as the mean ± SD (n = 5). Statistical significance was calculated via one-way ANOVA (panels c-j) in GraphPad Prism. * $p < 0.05$, ** $p < 0.01$, *** $p < 0.001$, and **** $p < 0.0001$.

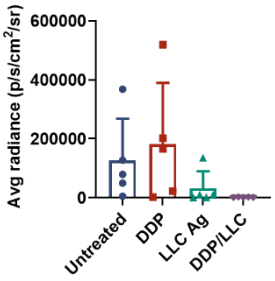

Figure S18. Statistical data showed the fluorescence intensity of Figure 5b at day 24 (n = 5).

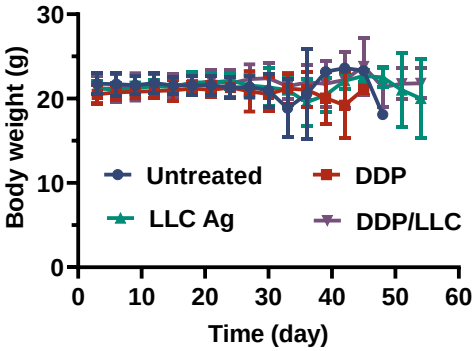

Figure S19. The body weight of mice after different treatments in prophylactic experiment.

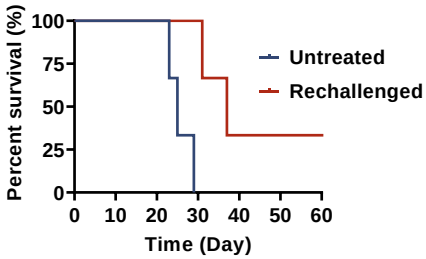

Figure S20. Survival curves of mice bearing LLC-Luc tumors with different treatments (n = 3).

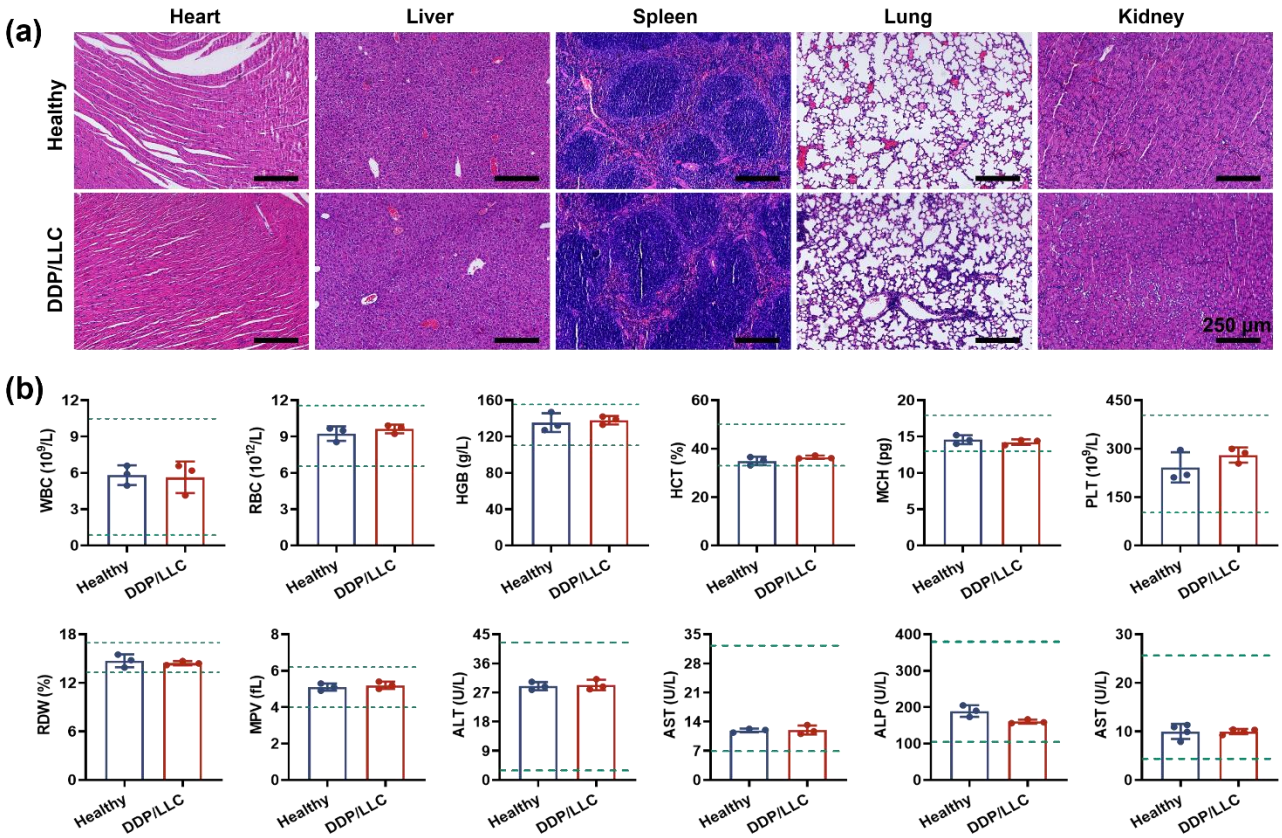

Figure S21. (a) H&E staining of heart, liver, spleen, lung and kidney from mice in healthy and DDP/LLC groups. Scale bars: 250 μm. (b) Blood biochemistry and complete blood analysis of mice after receiving DDP/LLC immunization (n = 3). The following parameters were tested: white blood cell (WBC) counts; red blood cell (RBC)

counts; haemoglobin (HGB); haematocrit value (HCT); mean corpuscular haemoglobin (MCH) and platelets (PLT); red cell volume distribution width (RDW); mean platelet volume (MPV); alanine aminotransferase (ALT); aspartate aminotransferase (AST); alkaline phosphatase (ALP); blood urea nitrogen (BUN).

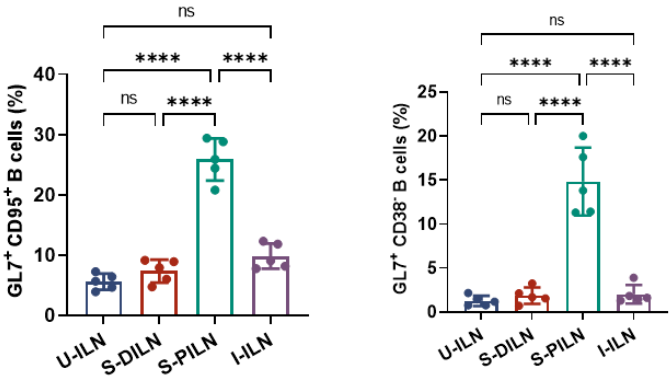

Figure S22. The statistical data shows the proportion of the activated germinal center B cells in thoracic lymph nodes after immunization with different strategies (n = 5). Note: Untreated group-Inguinal lymph nodes (U-ILN), Subcutaneous immunization group-Distal inguinal lymph nodes (S-DILN), Subcutaneous immunization group-Proximal inguinal lymph nodes (S-PILN), inhaled immunization group-Inguinal lymph nodes (I-ILN). Data are presented as the mean ± SD (n = 5). Statistical significance was calculated via one-way ANOVA in GraphPad Prism. * $p < 0.05$, ** $p < 0.01$, *** $p < 0.001$, and **** $p < 0.0001$.

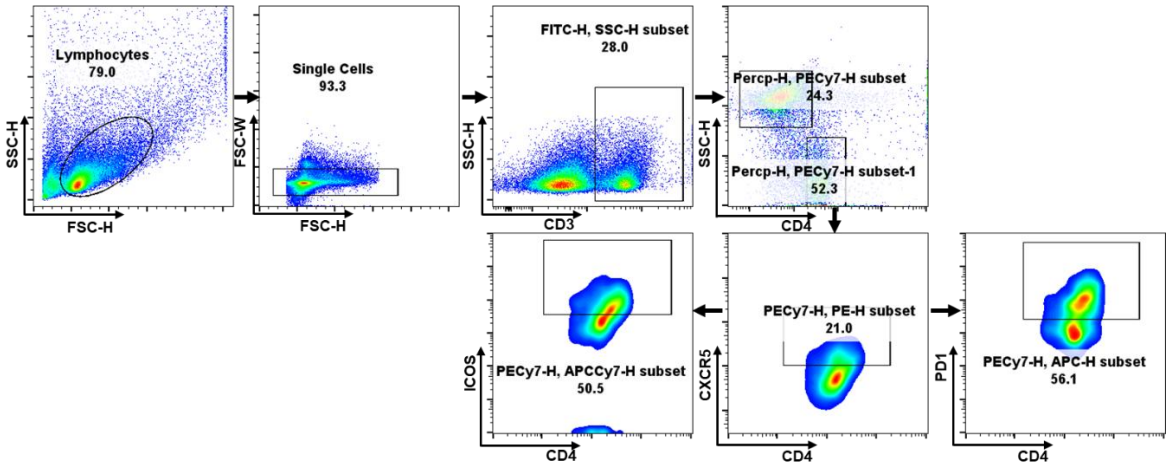

Figure S23. Flow cytometry gating strategy for the analysis of follicular helper T (Tfh) cells.

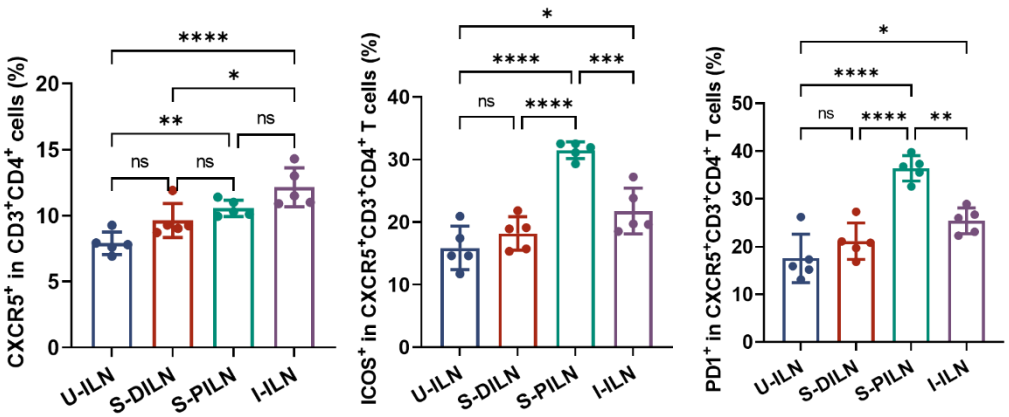

Figure S24. The statistical data shows the proportion of ICOS, CXCR5 and PD1 Tfh cells after immunization with different strategies (n = 5). Note: Untreated group-Inguinal lymph nodes (U-ILN), Subcutaneous immunization group-Distal inguinal lymph nodes (S-DILN), Subcutaneous immunization group-Proximal inguinal lymph nodes (S-PILN), inhaled immunization group-Inguinal lymph nodes (I-ILN). Data are presented as the mean ± SD (n = 5). Statistical significance was calculated via one-way ANOVA in GraphPad Prism. * $p < 0.05$, ** $p < 0.01$, *** $p < 0.001$, and **** $p < 0.0001$.

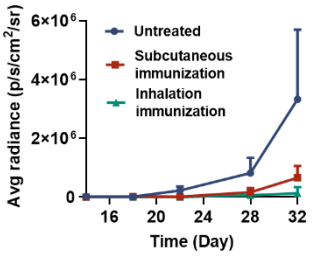

Figure S25. Statistical fluorescence intensity of tumor after different treatments (n = 5).

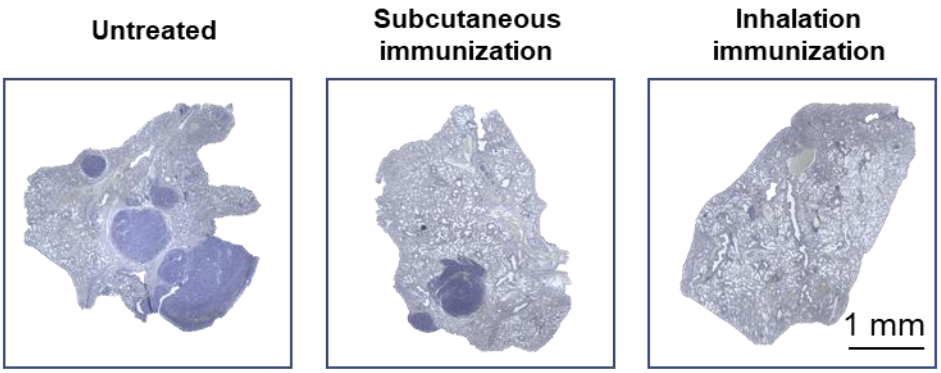

Figure S26. The hematoxylin and eosin (H&E) staining of lung tissue with different immunization strategies.

Table S1. DDP with different PBA substitutions.

Polymer	Glu/PBA ratio	PBA degree
DDP100	1/1	95
DDP50	1/0.5	46
DDP25	1/0.25	23

Table S2. OVA loading efficiency and encapsulation efficiency of DDP/OVA nanovaccine.

DDP/OVA (mass ratio)	OVA loading/ %	OVA encapsulation efficiency/ %
1/1	97.7	49.4